Stochastic perturbations in chaotic billiards

Jorge C. Leitão

Supervisors: João P. Viana and Eduardo G. Altmann

Mestrado em Física

Departamento de Física e Astronomia, Setembro de 2012

From the proudest son, to my mother.

Acknowledgements

I would like to thank both of my supervisors, Eduardo G. Altmann and João P. Viana, for their patience and teachings. In particular, I would like to thank João P. Viana for the huge effort he invested on me. The third chapter of this thesis was his idea and all the knowledge I have on computational physics is due to him, and most of the work done in that chapter would not have been possible without him either. Also, I want to emphasize that the possibility to work at the Max Planck Institute with Eduardo G. Altmann, gave me a much broader perspective on how to approach a problem. Moreover, I have learned about the major role played in science by the so called "soft skills": the importance of expressing ideas correctly, the ability to manage time and organize work, being aware of the different groups working on similar subjects, as well as being updated about the recent literature, etc. Eduardo G. Altmann was fundamental in all of this and I'm very thankful for the opportunity he gave me.

I acknowledge the Erasmus scholarship 29233-IC-1-2007-1 -PT-ERASMUS-EUCX-1 for the financial support during the five months of Erasmus placement, and Otto Hahn Junior Research Group of the Max Planck Institute for the Physics of Complex Systems (PKS@MPI) for the important support on my first month in Dresden, and PKS@MPI for the excellent conditions provided during my stay there.

Abstract

Transient chaos has been receiving increasing attention due to its applications in fluid dynamics, dye boundaries, advection, chemical reactions, etc. In this thesis, we focus on two fundamental topics of transient chaos: random perturbations of deterministic trajectories in open billiard systems and efficient sampling of initial conditions.

To study random perturbations of deterministic trajectories, we numerically compute the survival probability of trajectories in a mixed phase space open billiard with noise-perturbed trajectories. On Ref. [1], it was shown that noise can increase the life-time of trajectories in area-preserving chaotic systems. Here, we generalize these results to mixed phase space billiard systems. We also show that, for small noise intensities, the escape rate due to noise scales with noise intensity squared. For sufficiently high noise intensities, this escape rate has a cutoff at the escape rate obtained in the non-perturbed system. We believe that our results can have practical implications, for instance, in the study of laser cavities. These findings were published in Ref. [2].

One current problem of numerically computing quantities in transient systems is that most methods are exponentially slow with increasing escape time. In this thesis, we use the Landau algorithm[3] and show that it is possible to compute the escape time distribution in polynomial time, much faster than the current methods. We show that, for an efficient sampling, the proposal function of the Monte Carlo process must scale the maximum Lyapunov exponent, a fundamental property of the dynamical system. We present a new algorithm that computes both the escape time distribution and the desired proposal function in both area preserving maps and higher dimensional systems with dimensions at least 4. We argue that numerical simulations in transient chaos can highly benefit from our method.

We show the problems of extending these results to non-hyperbolic Hamiltonian systems.

Resumo

O caos transiente tem recebido crescente atenção devido às suas aplicações em dinâmica dos fluidos, fronteiras de tintas, advecção, reacções químicas, etc. Nesta tese, focamo-nos em dois tópicos fundamentais do caos transiente: perturbações aleatórias em bilhares abertos e amostragem eficiente de condições iniciais.

Para estudar perturbações aleatórias de trajetórias deterministicas, calculamos a probabilidade de sobrevivência de trajetórias perturbadas com ruído num bilhar aberto com espaço de fase misto. Na Ref. [1] foi mostrado que o ruído pode aumentar o tempo de vida das trajetórias em sistemas caóticos que preservam àrea. Nós generalizamos esses resultados para bilhares de espaço de fase misto. Mostramos que para baixas intensidades, a taxa de escape devido ao ruído aumenta quadraticamente com a intensidade do ruído. No entanto, para ruído elevado, esta taxa de escape é limitada pela taxa de escape do bilhar não perturbado. Acreditamos que os nossos resultados podem ter aplicações práticas, por exemplo, no estudo de cavidades laser. Estes resultados foram publicados na Ref. [2].

Um problema importante ao calcular numericamente quantidades em sistemas transientes é que a grande maioria dos métodos é exponencialmente lento com o aumento do tempo de escape. Nesta tese usamos o algoritmo de Landau[3] e mostramos que é possível calcular a distribuição de tempos de escape em tempo polinomial, muito mais eficiente que os métodos usados hoje em dia. Mostramos que para uma amostragem eficiente, a função proposta do processo de Monte Carlo tem de escalar com o expoente de Lyapunov, uma propriedade fundamental do sistema dinâmico. Apresentamos também um novo algoritmo que calcula não só a distribuição de tempos de escape como também a função proposta que garante eficiência, tanto em mapas que preservam a área como em sistemas de pelo menos

4 dimensões. Acreditamos que simulações numéricas em caos transiente podem beneficiar imenso com o nosso método.

Por fim, listamos alguns problemas em generalizar o método para sistemas hamiltonianos não hiperbólicos.

Contents

Chapter 1

Introduction

1.1 Introduction to dynamical systems

1.1.1 Hamiltonian systems

A dynamical system is defined as a set of deterministic variables, $\boldsymbol{r}$, described by an evolution equation

$$\frac{d\boldsymbol{r}}{dt} = \boldsymbol{F}(\boldsymbol{r}, t)$$

where $\boldsymbol{r} \in \Omega$, Ω is the phase space of the dynamical system and $\boldsymbol{F}(\boldsymbol{r}, t)$ is a vectorial function.

We will focus in *time independent Hamiltonian systems*, systems that are completely described by the scalar function $H(\boldsymbol{r})$, the Hamiltonian. Let $\boldsymbol{r} = (\boldsymbol{p}, \boldsymbol{q}) \in \mathbb{R}^N \times \mathbb{R}^N = \mathbb{R}^{2N}$ the set of variables that completely describe the system, in which $\boldsymbol{q}$ e $\boldsymbol{p}$ are $2N$ coordinates (the position and the conjugate momentum of the system). An Hamiltonian system is one in which

$$\boldsymbol{F}(\boldsymbol{r}) = S_N \cdot \partial_{\boldsymbol{r}} H(\boldsymbol{r}) \tag{1.1}$$

where

$$\partial_{\boldsymbol{r}} H(\boldsymbol{r}) \equiv \begin{bmatrix} \partial_{\boldsymbol{p}} H(\boldsymbol{p}, \boldsymbol{q}) \\ \partial_{\boldsymbol{q}} H(\boldsymbol{p}, \boldsymbol{q}) \end{bmatrix}$$

and S_N a matrix defined by

$$S_N = \begin{bmatrix} O_N & -I_N \\ I_N & O_N \end{bmatrix}.$$

where O_N is the $N \times N$ null matrix, and I_N is the $N \times N$ identity matrix. One of the main properties of an Hamiltonian system is the preservation of the phase space volume, a consequence of null divergence of $\boldsymbol{F}(\boldsymbol{r})$:

$$\frac{\partial}{\partial \boldsymbol{r}} \cdot \boldsymbol{F}(\boldsymbol{r}) = \frac{\partial}{\partial \boldsymbol{p}} \left(-\frac{\partial H}{\partial \boldsymbol{q}} \right) + \frac{\partial}{\partial \boldsymbol{q}} \left(\frac{\partial H}{\partial \boldsymbol{p}} \right) = 0$$

We also notice that the time evolution of the volume inside a closed surface of the phase space, S_0, is null:

$$\frac{d}{dt}\int_{S_0} d^{2N}\boldsymbol{r} = \int_{S_0} \frac{d\boldsymbol{r}}{dt} d\boldsymbol{S} = \int_{S_0} \boldsymbol{F}\cdot d\boldsymbol{S} = \int_{S_0} \frac{\partial}{\partial \boldsymbol{r}}\cdot \boldsymbol{F} d^{2N}\boldsymbol{r} = 0$$

which is the well known *Liouville theorem.*

However, the most fundamental structure of the Hamiltonian system is that it is sympletic[4]. Consider the three trajectories

- $(\boldsymbol{p}(t), \boldsymbol{q}(t))$
- $(\boldsymbol{p}(t) + \delta\boldsymbol{p}(t), \boldsymbol{q}(t) + \delta\boldsymbol{q}(t))$ and
- $(\boldsymbol{p}(t) + \delta\boldsymbol{p}'(t), \boldsymbol{q}(t) + \delta\boldsymbol{q}'(t))$

where $\delta\boldsymbol{p}, \delta\boldsymbol{q}, \delta\boldsymbol{p}', \delta\boldsymbol{q}'$ are infinitesimal column vectors. A system is said sympletic if and only if

$$\frac{d}{dt}\left(\delta\boldsymbol{p}\cdot\delta\boldsymbol{q}' - \delta\boldsymbol{q}\cdot\delta\boldsymbol{p}'\right) = \frac{d}{dt}\left(\delta\boldsymbol{r}^\dagger\cdot S_N\cdot\delta\boldsymbol{r}'\right) = 0 \tag{1.2}$$

where † means transpose. We see that an Hamiltonian system is sympletic because

$$\begin{aligned}
\frac{d}{dt}\left(\delta\boldsymbol{r}^\dagger\cdot S_N\cdot\delta\boldsymbol{r}'\right) &= \frac{d\delta\boldsymbol{r}^\dagger}{dt}\cdot S_N\cdot\delta\boldsymbol{r}' + \delta\boldsymbol{r}^\dagger\cdot S_N\cdot\frac{d\delta\boldsymbol{r}'}{dt} \\
&= \left(\frac{\partial\boldsymbol{F}}{\partial\boldsymbol{r}}\cdot\delta\boldsymbol{r}\right)^\dagger\cdot S_N\cdot\delta\boldsymbol{r}' + \delta\boldsymbol{r}^\dagger\cdot S_N\cdot\left(\frac{\partial\boldsymbol{F}}{\partial\boldsymbol{r}}\cdot\delta\boldsymbol{r}'\right) \\
&= \delta\boldsymbol{r}^\dagger\cdot\left(S_N\cdot\frac{\partial^2 H}{\partial\boldsymbol{r}\partial\boldsymbol{r}}\right)^\dagger\cdot S_N\cdot\delta\boldsymbol{r}' + \delta\boldsymbol{r}^\dagger\cdot S_N\cdot\left(S_N\cdot\frac{\partial^2 H}{\partial\boldsymbol{r}\partial\boldsymbol{r}}\right)\cdot\delta\boldsymbol{r}' \\
&= 0
\end{aligned}$$

where the last equality comes from

$$\left(\frac{\partial^2 H}{\partial\boldsymbol{r}\partial\boldsymbol{r}}\right)^\dagger = \frac{\partial^2 H}{\partial\boldsymbol{r}\partial\boldsymbol{r}}$$

and

$$S_N\cdot S_N = -I_{2N},\ S_N^\dagger = -S_N\ .$$

As an example of an Hamiltonian system, we consider the two dimensional system characterized by a point ball inside a circumference-like wall, with specular reflections in the wall. The Hamiltonian of the system is

$$H(\boldsymbol{p},\boldsymbol{q}) = \frac{\boldsymbol{p}^2}{2m} + \begin{cases} 0 & if\ \ |\boldsymbol{q}|^2 \le 1 \\ \infty & else \end{cases} \tag{1.3}$$

where $\boldsymbol{q} = (x, y)$ and $\boldsymbol{p} = m(v_x, v_y)$, and we will call it our *toy model.* This system has $2N = 4$ degrees of freedom and energy conservation dictates that $\boldsymbol{p}^2 = const$, which we will use $\boldsymbol{p}^2 = 1$.

1.1.2 The Poincaré surface of section and sympletic maps

Given a dynamical system of $2N$ degrees of freedom, it is frequent to project it in a $2N-1$ space by considering the projection of the system's evolution over a surface of section of the phase space. It can be shown that this projection is well defined in Hamiltonian systems and this map is *sympletic*[4]. A map

$$\boldsymbol{r}_{n+1} = T\left(\boldsymbol{r}_n\right)$$

is called sympletic when the matrix $A = \partial T/\partial \boldsymbol{r}$ satisfies

$$S_N = A^\dagger \cdot S_N \cdot A \ . \tag{1.4}$$

A matrix that fulfills this condition is called a *sympletic matrix* and thus the map is called a sympletic map. It can be shown that sympletic maps are area-preserving[4] and that in two dimensions, area-preserving maps are also sympletic maps. One important property of sympletic matrices is that if λ is an eigenvalue of A, i.e. if it is a solution of

$$det\left(A - I\lambda\right) = 0 \ ,$$

using Eq. 1.4, we can compute

$$A = S_N^{-1}\left(A^\dagger\right)^{-1} S_N \tag{1.5}$$

and thus

$$\begin{aligned} det\left(A - I\lambda\right) &= det\left(S_N^{-1}\left(A^\dagger\right)^{-1} S_N - I\lambda\right) \\ &= det\left(\left(A^\dagger\right)^{-1} - I\lambda\right) \\ &= det\left(A^{-1} - I\lambda\right) \end{aligned}$$

which means that the eigenvalues of A and A^{-1} are the same. Because they are the inverses of each other, the only possible solution is the eigenvalues of A to occur in pairs (λ, λ^{-1}).

We now look at our toy model, and we present an example of a surface of section, in this case the constraint $x^2 + y^2 = 1$. This surface of section considers the particular times on which the particle hits the boundary. It is easy to see that the angle of incidence does not vary in time; so, in total, there are 2 time independent quantities: the energy and the angle of incidence, and we are restricting the phase space to $|\boldsymbol{q}| = 1$. With these three constraints, we can write the Hamiltonian in a map of $2N - 3 = 1$ time dependent coordinates. One way this can be achieved is to consider

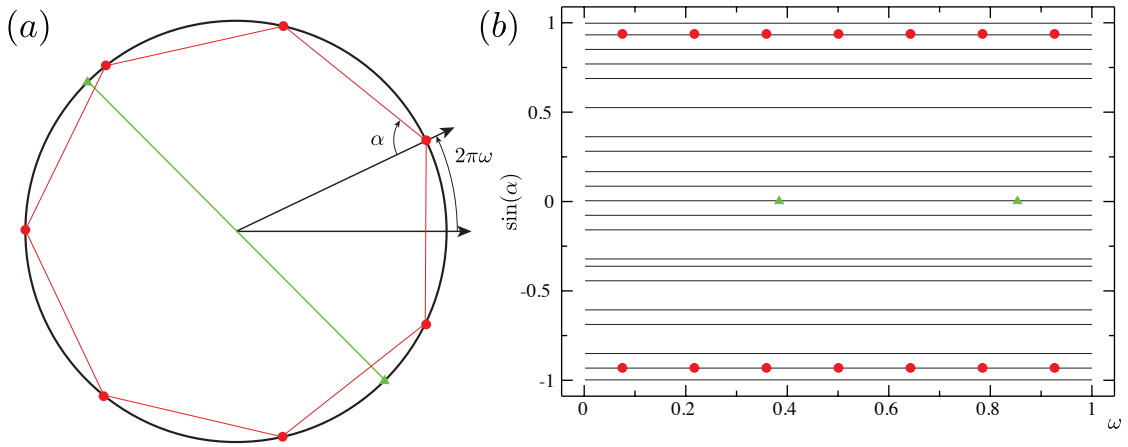

Figure 1.1: (Color Online) Circular billiard in Birkhoff coordinates. (a) Representation of the billiard table. (b) Phase space representation. The red dots represent a period 6 periodic orbit, and in green triangles the period 2. Black lines in the phase space represent orbits that have $w \notin \mathbb{Z}$. They asymptotically fill the whole line.

the Birkoff coordinates, which are also area-preserving[5]. The Birkoff coordinates can be expressed as $(\omega, \sin\alpha)$, $\omega \in [0, 2\pi]$ and $\sin\alpha \in [-1, 1]$ where ω is the angle in the boundary and α is the angle of reflection as shown in figure 1.1. Notice that because of the angle of incidence conservation, α is constant. Using Birkoff coordinates, the discrete map is called the circurlar billiard map and can be written as[5]

$$T(\omega_n) : \begin{cases} \alpha_{n+1} &= \alpha_n \\ \omega_{n+1} &= \omega_n + (\pi - 2\alpha_n) \end{cases} . \tag{1.6}$$

One interesting feature of this map is that if the initial α is such that the number

$$w \equiv \frac{\pi}{2\alpha} \in \mathbb{Z} \tag{1.7}$$

then any initial condition ω_0 leads to a periodic orbit. For instance, if $\alpha = \pi/3$,

$$\omega_{n+6} = \omega_n + 6\left(\pi - \frac{2\pi}{3}\right) = \omega_n + 2\pi = \omega_n \ ,$$

i.e. the orbit draws an hexagon inscribed inside the circle, as represented in the figure 1.1. So, even in this simple example we can distinguish two kinds of orbits: the periodic ones, for $w \in \mathbb{Z}$ and the ones called *quasi-periodic*, when $w \notin \mathbb{Z}$, which are aperiodic and asymptotically visit the interval $[0, 2\pi]$ in ω. Their representation in the billiard are polygons which tilt a bit for each new complete rotation in the circle; in the phase space, these aperiodic orbits are represented by lines, as in Fig. 1.1(b). We can also see that periodic orbits of the flow are fixed points of the map, and aperiodic orbits of the flow are lines in the map's phase space.

1.1.3 Stability of sympletic maps

We now provide some general results in the stability of the periodic orbits, and for simplicity we restrict ourselves to the 2-dimensional maps. A point $\boldsymbol{r}^*$ in the phase space is called a fixed point if

$$T(\boldsymbol{r}^*) = \boldsymbol{r}^* \tag{1.8}$$

and a periodic orbit of period n is such that every point in the orbit fulfills

$$T^n(\boldsymbol{r}^*) = \boldsymbol{r}^*$$

where the upper script n is to be read as the n-th iteration of the map. As we have seen in the toy model, the hexagon is an example of a periodic orbit. Also, notice that a periodic orbit of period n is a fixed point of the map T^n, thus we can restrict the study of the linear stability to fixed points. Because the map T is sympletic, T^n is also sympletic[4] and so both their eigenvalues occur in pairs (λ, λ^{-1}). This means that, for 2-dimensional area-preserving maps, the eigenvalues of the matrix $A^* = \partial T^n / \partial \boldsymbol{r}(\boldsymbol{r}^*)$ can only be of one of the two cases:

1. both roots are real, λ, λ^{-1} or
2. both roots are complex numbers in unit circle, $\lambda, \lambda^{-1} = \exp(\pm i\theta)$.

In the first case, orbits nearby the fixed point asymptotically converge (diverge) to the fixed orbit by the direction of the eigenvector associated to $|\lambda| < 1$ ($|\lambda| > 1$). These fixed points are called *hyperbolic fixed point*. The origin of the word hyperbolic is clear when we represent it in figure 1.2 along with some trajectories. In the second case, nearby orbits rotate around the fixed point.

1.1.4 Manifolds and hyperbolicity

The stable(unstable) manifold of an hyperbolic point is defined as the set of points in the phase space that asymptotically converge(diverge) to it[4]. The relevance of hyperbolic point is that important mathematical results can be derived in its vicinity[4, 5], which greatly simplifies its study. We will later see some of these results.

Given an hyperbolic point, one can ask to what extent the stable and unstable manifolds intersect each other. In Hamiltonian systems, two stable manifolds cannot intersect each other. If it was not so, a forward iteration in time would have two solutions, which is not possible by the uniqueness of Hamilton equations. Similar arguments apply for two unstable manifolds in inverse time. However, a stable manifold

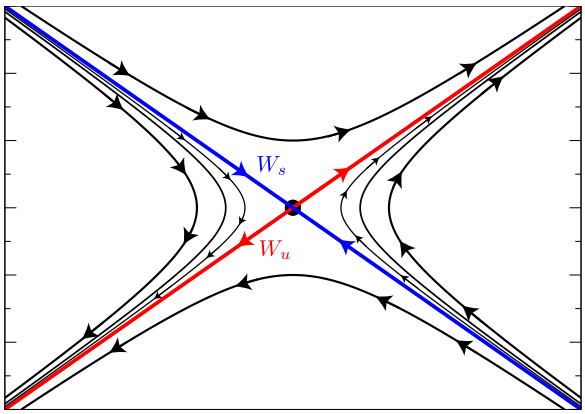

Figure 1.2: (Color Online) Representation of an hyperbolic fixed point (black dot at center) and some trajectories that pass close of it. Also depicted in figure, the stable W_s (blue) and unstable W_u (red) manifold, which are tangent to the eigenvector associated with the $|\lambda| < 1$ and $|\lambda| > 1$ respectively.

can intersect an unstable manifold. This intersection is called an *homoclinic point*, and if one exists, there are infinitely many[6, 4]. To see this, first, we have to notice that a forward iteration of a point in both the stable and unstable manifold must also be in both the stable and unstable manifold. Then, an iteration of a point belonging to the two manifolds must also belong to both of them. It can be shown that between an homoclinic point γ and its first iteration, $T(\gamma)$, must also exist another homoclinic point[6]. This leads to a complicated arrangement of the manifolds, exemplified in figure 1.3.

1.1.4.1 Hyperbolic chaos

Chaos, defined as a sensitive dependence on initial conditions, is a phenomenum closely related to the concept of hyperbolic points. Before we explain its origin in dynamical systems, we provide a simple example of an area-preserving map that exhibits chaos. Consider a baker, and the typical movement he makes to mix the several ingredients of the bread. This movement can minimally be described by two different actions: first the baker stretches the dough in one direction, and then he folds it onto the dough itself. This process of stretching and folding can be written as a map, called the baker map, which is a paradigmatic example of a two dimensional

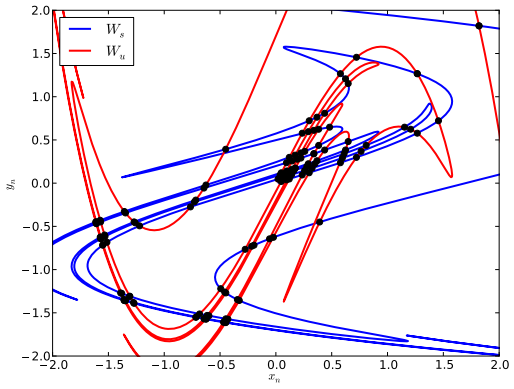

Figure 1.3: (Color Online) Complicated arrangement of the homoclinic intersections (black dots) of the stable (W_s) and unstable (W_u) manifold, of the discrete nonlinear Schrödinger equation, retrieved from Ref. [7].

hyperbolic area preserving map[4]. The map is defined by

$$T: \begin{cases} \begin{cases} x_{n+1} &= x_n/2 \\ y_{n+1} &= 2y_n \end{cases} & if\ y_n \leq 1/2 \\ \begin{cases} x_{n+1} &= 1/2 + x_n/2 \\ y_{n+1} &= 2y_n - 1 \end{cases} & if\ y_n > 1/2 \end{cases}$$

in the square $[0,1] \times [0,1]$. It has two fixed points, the $(0,0)$ and $(1,1)$. One notices that the points in $(0, 0^+)$ are repelled from $(0,0)$, while points in $(0^+, 0)$ are attracted to $(0,0)$, and thus the stable manifold is tangent to $\boldsymbol{u}_s = (1,0)$, and the unstable manifold to $\boldsymbol{u}_u = (0,1)$ near $(0,0)$. Moreover, two points that start close to each other will always exponentially diverge: given $\boldsymbol{r}$ and $\boldsymbol{r} + \boldsymbol{\varepsilon}$, one iteration of the map will always make the y component of $\boldsymbol{r}$ to exponentially increase (with exponent $\log 2$), and thus $\boldsymbol{\varepsilon}_y$ will be further and further amplified. For instance, if $\boldsymbol{\varepsilon}_y = 2^{-20}$, after 19 iterations, $\boldsymbol{\varepsilon}_y = 2^{-1}$, and thus the two initial conditions are now far away from each other, the reason of the expression "sensitive dependence in the initial conditions". Formally, a system can be defined as chaotic if it has a positive *Lyapunov exponent*[4]. The Lyapunov exponent is defined as the average exponent of divergence of initial conditions[4],

$$\lambda(\boldsymbol{u}_0) = \frac{1}{V_{phase-space}} \int_{phase-space} d\boldsymbol{r} \frac{1}{n} \log \left| \frac{\partial T^n(\boldsymbol{r})}{\partial \boldsymbol{r}} \cdot \boldsymbol{u}_0 \right| \tag{1.9}$$

where $\boldsymbol{u}_0$ is unitary vector defining the direction from which the Lyapunov exponent is being calculated. From the definition, if the maximum Lyapunov is positive, the map is chaotic. In this map, the Lyapunov exponent in the direction $\boldsymbol{u}_0 = \hat{y}$ is $\log 2$

which allow us to conclude that the baker map is chaotic. It can be shown that if the map is area-preserving the sum of Lyapunov exponents must be null[4]. The other Lyapunov exponent of this system is the one with $\boldsymbol{u}_0 = \hat{x}$, which is $\log 2^{-1} = -\log 2$, as it should. Thus, in a two-dimensional area preserving map, either both Lyapunov exponents are zero, or they occur in pairs $\pm\lambda$.

Smale[8] has shown that the existence of homoclinic points leads to a dynamics that can be represented by the same type of dynamics of the baker's map[1], thus showing chaotic behavior. One can then characterize chaos as a consequence of a stretching and folding mechanism, which causes small errors to be amplified.

1.2 Chaotic and regular motion in mixed phase space systems

In our toy model, we were able to re-write the map in a very simple formulation (Eq. 1.6) and clearly not showing any chaotic behavior. One natural question is when is this possible. In this section we provide some insight in what is integrability, and why it is important in ruling out chaoticity of a system.

We start with the concept of *constant of motion*, which is any quantity $f(\boldsymbol{p}, \boldsymbol{q})$ that does not vary under the action of the map or flow. The most prominent example of a constant of motion in time independent Hamiltonian systems is the Hamiltonian itself, which is constant equal to the total energy of the system. Generically, we can write the total time derivative of f as

$$\frac{df}{dt} = \frac{d\boldsymbol{p}}{dt}\frac{\partial f}{\partial \boldsymbol{p}} + \frac{d\boldsymbol{q}}{dt}\frac{\partial f}{\partial \boldsymbol{q}} = \frac{\partial H}{\partial \boldsymbol{p}}\frac{\partial f}{\partial \boldsymbol{q}} - \frac{\partial H}{\partial \boldsymbol{q}}\frac{\partial f}{\partial \boldsymbol{p}} \equiv \{f, H\}$$

where $\{\cdot, \cdot\}$ is the Poisson brackets. This means that f is a constant of motion if and only if

$$\{f, H\} = 0 \ .$$

A Hamiltonian system is called integrable when one can find N independent constants of motion, f_i, such that

$$\{f_i, f_j\} = 0 \ \forall i, j = 1, ..., N$$

[1]Rigorously, Smale showed that the homoclinic points lead to equivalent dynamics of the Smale horseshoe map, which in turn can be represented by a symbolic dynamics. Baker's map can also be represented via symbolic dynamics, and thus for practical reasons has the same features as the horseshoe map. We have used Baker's map because it will later be used in this thesis.

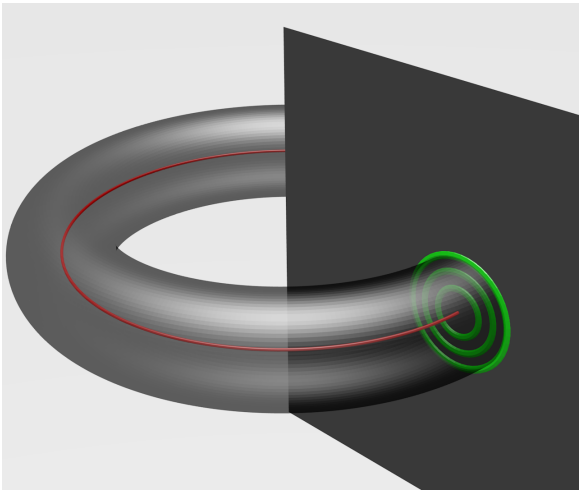

Figure 1.4: (Color) Schematic representation of a 2-dimensional torus in a generic 3D space and the respective continuous variation of the coordinates θ_1 (red) and θ_2 (green). The system moves freely on the surface of the torus. The torus' big radius is given by ω_1 and the smaller by ω_2. The plane represents a surface of section $\theta_1 = 2\pi$.

where $f_1 = H$. This definition is motivated by the fact that, when we are able to find those f_i, it can be shown[4] that it is possible to perform a canonical change of variables such that, in the new set of coordinates, $(\boldsymbol{I}, \boldsymbol{\theta})$, the solution of the system is

$$\begin{cases} \boldsymbol{I}(t) & = \boldsymbol{I}(0) \\ \boldsymbol{\theta}(t) & = \boldsymbol{\theta}(0) + \boldsymbol{\omega}(I)\, t \mod 2\pi \end{cases} \tag{1.10}$$

where

$$\boldsymbol{\omega}(I) = \frac{\partial H'}{\partial \boldsymbol{I}}$$

and H' is the Hamiltonian in the new set of variables $(\boldsymbol{I}, \boldsymbol{\theta})$. Because $\boldsymbol{\omega}$ does not depend on time, the movement is very simple. It can be viewed as a movement restricted to a N-dimensional toroidal surface in the phase space, represented in figure 1.4. The analogy to a simple rotation is clear if we interpret θ as an angle and ω as an angular frequency. Our toy model is a clear example of an integrable system. We have 2 constants of motion in a 4 dimensional Hamiltonian system and thus we were able to write the discrete map which, when solved for an arbitrary n, is of the form 1.10. An integrable system is naturally non-chaotic because the maximum Lyapunov exponent is zero.

1.2.1 KAM Theorem and non-hyperbolic components

A fundamental question in this image of integrable Hamiltonian system is whether the system stays integrable after a perturbation. Komogorov, Arnold and Mosser

built, between 1954 and 1973, the KAM theorem where they presented a very general framework to test the integrability of dynamical systems. In general lines, they have shown that, for small ε, most of the unperturbed tori survive. I.e. the set of tori that does not survive is a set of zero measure. However, this set is dense in the phase space and suffers dramatic changes.

The KAM theorem shows that the tori whose orbits are periodic (those that satisfy Eq. 1.7 in the toy model) are those that suffer fundamental changes in the dynamics. The infinitesimal perturbation destroys those tori and creates a set of elliptical and hyperbolic points[4] around them. The non-triviality comes from the fact that these new elliptic points also bifurcate because of the perturbation, generating a new set of elliptical and hyperbolic points, leading to an *ad infinitum*[4] cascade. The final outcome can be seen as an hierarchic structure with a depth: the "first" set of periodic points was destroyed and created a "second" set which creates a "third" set, etc. These complicated structures, formed around each periodic orbit, are called *KAM islands*. It can also be shown that on each hierarchic structure there is also chaos[4, 6] due to the generated hyperbolic points inside them.

As a picture of the phenomena, we present the changes of the phase space of the kicked rotor: a bar with moment of inertia $\overline{I}$ and length l, fastened to a frictionless pivot in one side and free in the other. This rotor is subject to a periodic kick of strength K/l at times $t = \tau, 2\tau, 3\tau, ..., n\tau$. The Hamiltonian of the system is

$$H\left(p_\theta, \theta, t\right) = \frac{p_\theta^2}{2\overline{I}} + K\cos\theta \sum_n \delta\left(t - n\tau\right)$$

which means that this Hamiltonian system is not energy conserved if $K \neq 0$. With natural units $\tau/\overline{I} = 1$, one can use a surface of section at time $t = n\tau$ to obtain the map[4]

$$\begin{cases} \theta_{n+1} &= (\theta_n + p_n) \bmod 2\pi \\ p_{n+1} &= p_n + K\sin\theta_{n+1} \end{cases}.$$

In figure 1.5 the phase space of the kicked rotor is shown for six different values of K in the six top panels. For $K = 0$, the tori are unperturbed and the system is integrable. With increasing K, some tori are destroyed and a KAM island is formed around the period 1 periodic orbit. As K is increased, more and more islands around points with increasing period are formed. Notice that magnifications of a periodic orbit (two bottom panels) would lead to the same picture due to the hierarchic structure explained before. In our language, each magnification would be looking for a different depth.

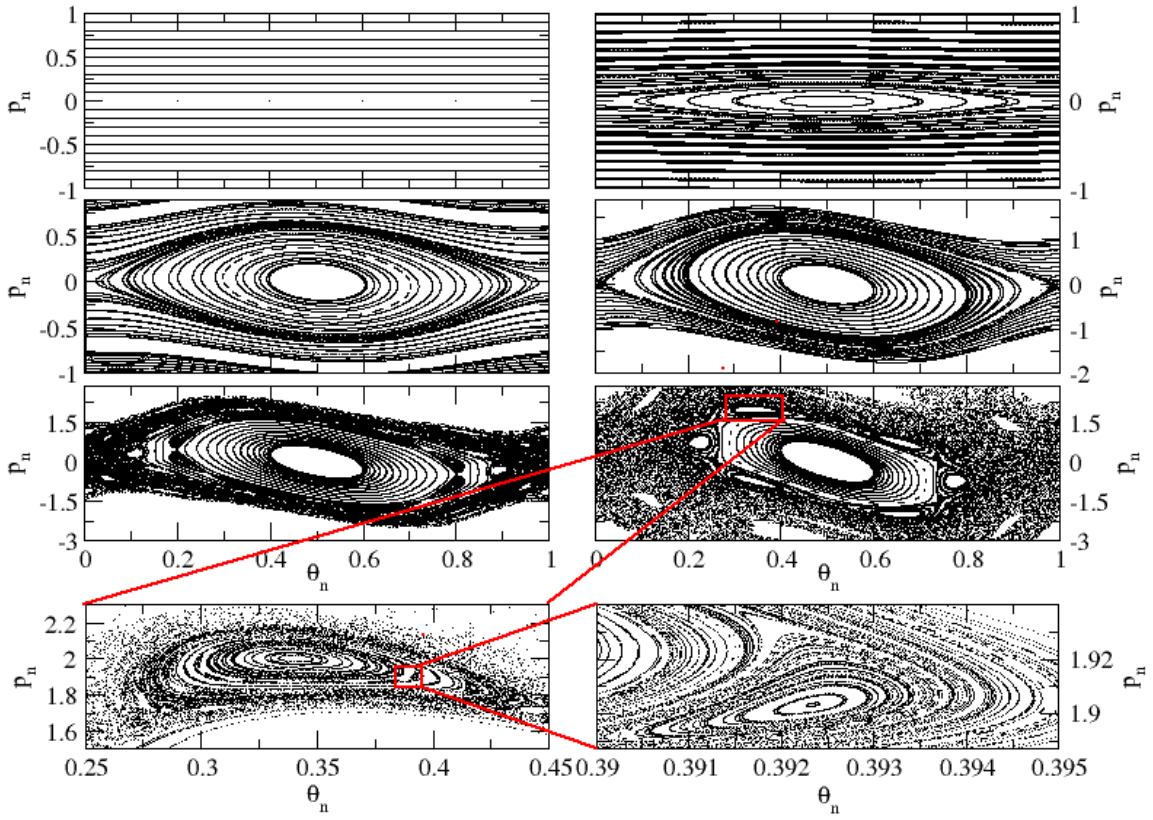

Figure 1.5: (Color Online) The phase space in the variables $(p_n, \theta_n/2\pi)$ of the kicked motor for 6 values of K. top left $K = 0$ (integrable), top right $K = 0.01$, middle-up left $K = 0.1$, middle-up right $K = 0.5$, middle-down left $K = 1$, middle-down right $K = 1.5$. Bottom left is an amplification of the middle-down right, and bottom right an amplication of the bottom left. Notice the formation of the hyperbolic and elliptic points around the central island is clear in the $K = 1.5$ panel, where one can distinguish 6 elliptic points and hyperbolic points and that further amplications of them lead to the same picture. The dotted area represents the chaotic component.

KAM islands are non-hyperbolic components which affect the dynamic of the chaotic trajectories. Without further details, which we refer to Refs. [4, 9, 6, 10], we would like to note that several models[9, 11, 12] were developed to study these structures and they predict that orbits that pass close by these KAM islands suffer from *stickiness*[13, 9, 14, 15]: once a chaotic orbit approaches these regions, it tends to stick near them. The stickiness appears due to the trapping of orbits in the boundary of a KAM island[9, 6]. This trapping is essentially due to the arrangement of semi-boundaries (also called *cantorus*), close to the KAM island. These semi-boundaries were tori that were broken by the perturbation. The fundamental change is that these semi-boundaries, contrary to a tori, allow the passage of orbits within it and so a *flux* can be defined on it as the number of orbits that can pass per area per unit of time. However, given the hierarchic structure presented in Sec. 1.2.1, several arguments lead to the conclusion that the scaling of this flux is a power-law (with negative exponent) with the depth of the island[9], i.e. the more in-depth the structure is, the smaller the flux is. This is a way of understanding stickiness in KAM islands[11, 12, 9, 6]: the greater the depth (in the hierarchic structure) the orbit is at, the more difficult it is to go to the next and more time it stays in that depth because the flux across the semi-boundaries is smaller and smaller.

We would like to emphasize that stickiness is not restricted to KAM islands. In general, non-hyperbolic components lead to stickiness of the orbits. Stickiness is defined when a region leads to a power-law behaviour of some properties (e.g. the recurrence time distribution) which would otherwise be exponential[15]. For instance, nearby the KAM islands, the Lyapunov exponent is zero as the divergence of initial conditions is power-law. Another example of non-hyperbolic components which also show stickiness are the marginally unstable periodic orbits (MUPOs)[16]. While these orbits have zero measure (contrary to the KAM islands), they also lead to a power-law behaviour of transport properties.

One important feature of the KAM islands and MUPOs is that they can be embedded in the hyperbolic chaotic component of the phase space (also called the chaotic sea). Motivated by this fact, systems haveing a coexistence of chaotic and non-chaotic trajectories in different components (of positive volume) of the phase-space are called *mixed phase-space* systems[4].

1.3 Open systems and transient chaos

So far, the systems we have discussed are closed: trajectories remain in a bounded region of the phase space. In this section we introduce the concept of transient chaos. Transient chaos occurs naturally in scattering problems: typically, a particle approaches a scattering region in a very simple movement, performs some chaotic movement inside the scattering region, and leaves it in another trivial movement. Transient chaos deals, for instance, with the chaotic movement in the scattering region and how it can affect the final outcome of the trajectory. Fluid dynamics, dye boundaries, advection, and chemical reactions are all examples that highly benefit from this framework[17, 4]. Another motivation of transient chaos is the connection between the properties of closed systems and open systems. For instance in our toy model (Eq. 1.3), if we insert a leak (a hole) in the boundary from where the particle could leave, the system becomes transient inside the circumference. However, the dynamics of the system in the limit the size of the leak going to zero approaches the dynamics of the closed system[18].

Perhaps the most important quantity that appears in open systems is the escape time distribution, $\rho(t)$[17]. Given an ensemble of initial conditions (e.g. uniformly distributed in the phase space), $\rho(t)$ is the relative number of them that escape at time t. The escape time distribution allow us to quantify the time-scale of the transient[17]. It also allows the study of closed systems for instance by its connection with the Poincaré recurrence time distribution[18].

1.3.1 Open hyperbolic systems

In open hyperbolic systems, the escape time distribution decays exponentially,

$$\rho(t) \propto e^{-\gamma t} \text{ for } t \to \infty \tag{1.11}$$

where γ is called the *escape rate*[17]. This scaling is the signature of chaoticity in open systems and defines the time-scale of the transient[17]. Notice that γ is the inverse of the characteristic time a particle stays in the transient and so is an important quantity to quantify the transient. A quantity closely related to $\rho(t)$ and often used is the *surviving probability*, which is the probability of a particle surviving until time t. It is given by the cumulative of $\rho(t)$,

$$P(t) = \sum_{t'=t}^{\infty} \rho(t')$$

and thus the main scalings of $\rho(t)$ are also present on $P(t)$[15]. We will use both $P(t)$ and $\rho(t)$ in this thesis.

An example of a chaotic hyperbolic system is the open baker map[17]. The open baker map is very similar to the baker map introduced in Sec. 1.1.4.1, and is defined by

$$\begin{cases} \begin{cases} x_{t+1} = cx_t \\ y_{t+1} = c^{-1}y_t \end{cases} & \text{if } y_t < 1/2 \\ \begin{cases} x_{t+1} = 1 - d(1 - x_t) \\ y_{t+1} = 1 - d^{-1}(1 - y_t)\, y_t \end{cases} & \text{if } y_t > 1/2 \end{cases}$$

in the unit square, $[0,1] \times [0,1]$ and $c, d < 1$, $c^{-1}/2 > 1$, $d^{-1}/2 > 1$ are the two parameters of the map. This map is schematically represented in Fig. 1.6 and consists in compressing the lower half part (below the dashed blue line) of the unit square in the x direction, and stretching it in the y direction, while the same is done in the upper part. In this thesis, we represent the two parameters of the map by the notation $\frac{1}{c}\&\frac{1}{d}$, i.e. for $c = 1/3$ and $d = 1/6$, we call it the 3&6 open baker map. This map is open as there are regions inside the unit square that are mapped outside it and thus leave, as represented in figure 1.6. The open baker map has the advantage that all the main quantities of interest can be analytically computed[17]. For instance, the region that does not escape after each iteration is $c + d$, which leads to an escape rate of[17]

$$\gamma = -\log(c + d). \tag{1.12}$$

One important question at this moment is whether every point leaves the system. The set of points of the phase space that never escape in neither forward nor backwards iterations of the map is called the *chaotic saddle*[17]; homoclinic intersections defined in Sec. 1.1.4 are part of this set. The name "chaotic saddle" is motivated by the same reasons of the name hyperbolic point in Sec. 1.1.4. In chaotic hyperbolic systems, the chaotic saddle is a zero measure set, i.e. the probability of a randomly chosen point in the phase space to be part of the chaotic saddle is null. Still, the chaotic saddle is important because it can be used to characterize all asymptotic properties of the *escaping* trajectories (e.g. the Lyapunov exponent). Moreover, the chaotic saddle is a fractal set, i.e. a set with non-integer dimension, $D_0 \notin \mathbb{N}$[17]. In the 3&3 open baker map the set of points that never leave the system in forward iterations is the middle third Cantor set(see Fig 1.6c) which has dimension $D_0 = \log 2/\log 3$[17]. While fractal sets have a subject on their own, they are strongly connected with dynamical systems[4]. Likewise, in open systems they also play an important role, as the chaotic saddle of a chaotic hyperbolic systems is a fractal set.

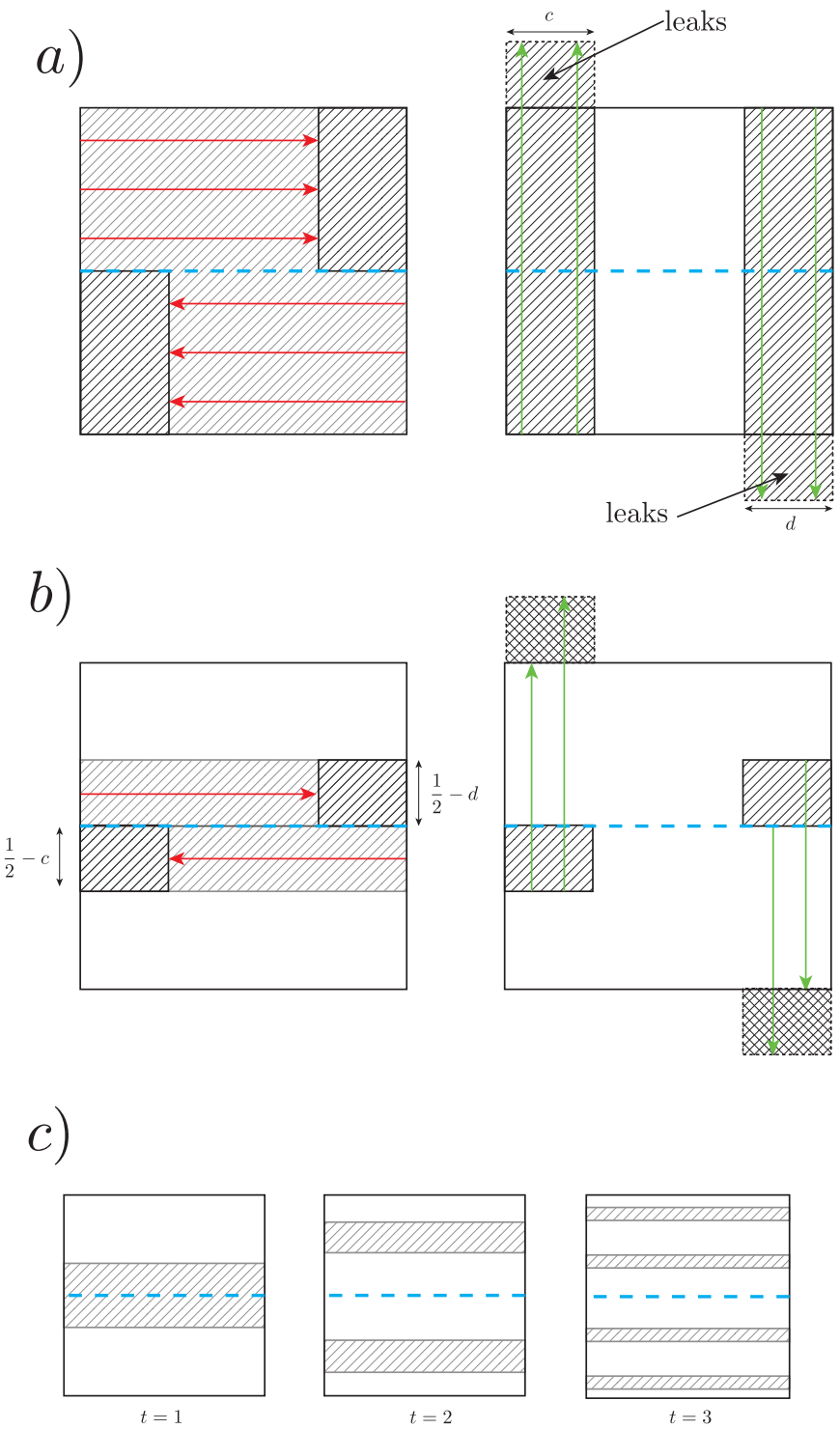

Figure 1.6: (Color Online) Schematic representation of the open baker map. a) an iteration of the full phase space; b) the iteration of the region that leaks on the first iteration. c) regions that leak at different iterations of the map. The colored arrows indicate the first iteration of the map with the compressing in red and the stretching in green.

One important relationship between the properties of the saddle and the properties of the open hyperbolic chaotic system is that the information dimension[17], D_1, of the chaotic saddle, is related to the escape rate and the Lyapunov exponent of the system[17],

$$D_1 = 1 - \frac{\gamma}{\lambda_1} \ , \tag{1.13}$$

where λ_1 is the positive Lyapunov exponent introduced in Sec. 1.1.4.1. For instance, in the open baker map, it can be shown to be[17]

$$\lambda_1 = \frac{c^{-1} \log d^{-1} + d^{-1} \log c^{-1}}{d^{-1} + c^{-1}} \ . \tag{1.14}$$

So, the dynamical properties of the system (γ, λ_1) are related with a property of the chaotic saddle, a property of a set. Another property which we will need is the metric entropy[17],

$$K_1 = \lambda_1 - \gamma \tag{1.15}$$

which is related with the growth of information of the measure[17].

Another advantage of the open baker map is that the chaotic saddle is a well known set, and thus allow important results to be derived. However, the most important advantage of the the open baker map is its generality: it is a paradigmatic example of chaotic open hyperbolic systems[17]; it has all the main features of them: fractal chaotic saddle, exponential decay of the escape time distribution, simple dynamics, etc. A more complicated example of a paradigmatic transient system is the Hénon map defined as

$$\begin{cases} x_{n+1} &= k - x_n^2 - y_n \\ y_{n+1} &= x_n \ . \end{cases} \tag{1.16}$$

Normally, one begins the initial conditions in the strip $I_{initial}$ defined by $x_i \in [0.9x_{fp}, 1.0x_{fp}]$ and $y_i = 0.9y_{fp}$ where $x_{fp} = y_{fp} = -1 - \sqrt{1+k}$ are the fixed points of the map. Like in the open baker map, almost all (except a set of zero measure) the orbits will eventually escape from region $x < 1.1x_{fp}$ and $y < 1.1y_{fp}$[10] if the map is hyperbolic. This map is a typical scattering problem where particles are being sent to the scatter in one direction, and are being scattered to another direction. In figure 1.7b, the escape time distribution as a function of x is plotted, calculated by sampling uniformly several hundred of particles inside $I_{initial}$. We can clearly see the fractality of the phase space in 1.7b, as a zoom of the picture gets the same picture *ad infinitum*. The reason for such high times in $I_{initial}$ is justified by the existence of an intersection of the stable manifold with the strip $I_{initial}$, depicted in Fig. 1.7a. The fractality is justified by the existence of an homoclinic intersection of the stable and unstable

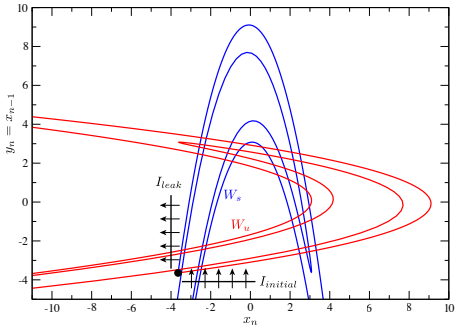

(a) (Color Online) Stable and unstable manifold of the Hénon map with $k = 6$ near the fixed point (black dot). The manifolds cross each other, leading to chaotic behavior of the map. The strip of initial conditions, $I_{initial}$, and exiting condition I_{leak} is also shown. Notice that W_s crosses I_{strip} infinite times, and this set is fractal, which is the reason why there is such a complex structure in Fig. 1.7b.

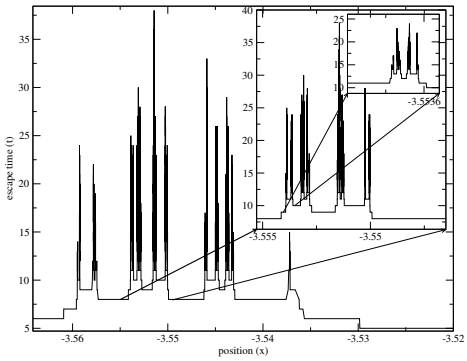

(b) Escape time distribution of initial conditions inside $I_{initial}$ that leave in I_{leak}. Because the stable manifold crosses $I_{initial}$ infinite times, there will be an infinite number of points which do not escape, which is a thin fractal set. Non-trivial behavior appears nearby those points. Further and further amplifications lead to the same picture, picture of fractal phase-space.

Figure 1.7: Representation of the hyperbolic Hénon map, Eq. 1.16 with $k = 6$.

manifold of the fixed point, also presented in figure 1.7a. For $k = 6$, the Hénon map is hyperbolic, with an escape rate of $\gamma \approx 0.64$.

1.3.2 Open non-hyperbolic systems

In non-hyperbolic systems, the picture gets more complicated because, as mentioned in Sec. 1.2.1, non-hyperbolic components like the borders of the KAM islands lead to stickiness of trajectories. One of the most important consequences of stickiness in open systems is that it changes the scaling of the escape time distribution from exponential to a power law decay for long time behavior:

$$\rho\,(t) \propto t^{-\beta}\ .$$

The question of whether the asymptotic regime has a well-defined and universal power law in the generic KAM case is still under investigation for area-preserving maps (see Refs.[11, 12] for the latest results that indicate $\beta \approx 2.57$). If no KAM islands are present, an exponent $\beta = 2$ can be obtained for MUPOs [19, 20, 21] (see Sec. 1.2.1). For simplicity we write the asymptotic decay as $t^{-\beta}$, but it is meant to describe the power-law like behavior usually observed in non-hyperbolic systems [13, 9, 14].

While in fully chaotic systems the chaotic saddle (Sec. 1.3.1) is a zero measure fractal set, in the case of non-hyperbolic systems the chaotic saddle can contain a

similar hyperbolic component[22, 18] but, additionally, it can include non-hyperbolic components like KAM islands. This means that typically there is a crossing over from exponential decay to power-law behaviour in these systems[18]. An example of an open non-hyperbolic system is the Hénon map with $k = 2$[10] as one of the fixed point is elliptic and forms KAM islands around it.

1.3.3 Open billiards

An important class of dynamical systems are the billiard systems. A billiard is a two-dimensional planar domain, in which a point particle moves with constant velocity inside it with specular reflections in the domain boundary. The toy model we have been discussing so far (see Fig. 1.1) is one of the simplest examples of a billiard. Billiard systems are naturally Hamiltonian because the boundary can be written as an Hamiltonian, like in Eq. 1.3. Recent literature has focused in open chaotic billiards due to the increasing interest in their applications[23, 24, 25]. For instance, a two-slab mirrored semi-conductor material can be perpendicularly excited and stimulated emission occurs in the parallel direction, creating a laser cavity. If we add a hole in the cavity, laser emission can be obtained from it. The shape of the cavity leads to different emission patterns, which can be studied by open classical billiards[26]. Moreover, from the theoretical point of view, open billiards have also been extensively studied[27, 28, 29, 20, 21], and constitute a paradigmatic class of Hamiltonian systems with mixed phase space: they can exhibit both integrable movement, periodic orbits, KAM islands, and chaotic behavior[15]. Thus, not only they are used to study particular devices, they are also used to study the general properties of mixed phase space Hamiltonian systems.

1.4 Focus of this thesis

In this thesis we investigate fundamental properties of open chaotic systems, having in mind numerical and experimental configurations of interest. We focus on two problems: the effect of white noise perturbations in mixed phase space billiard systems, and the problem of how to efficiently sample points in the phase space in order to achieve better statistics. In both problems the crucial step is to relate the previously discussed phase space structures (chaotic saddle, manifolds, KAM islands, etc.) to the quantities of interest in the problem (the survival probability in the case of noise perturbations and the sampling technique in the sampling problem). Analytical calculations are combined with numerical simulations in simple paradigmatic systems,

which show the generic properties of Hamiltonian transiently chaotic systems discussed in the previous sections.

We start with a characterization of the survival probability, both with and without noise. Our objective is to connect the different phase space components of the billiard with the different regimes of the survival probability and characterize how the noise changes them. One motivation to apply noise perturbations in billiard systems is to extend the unperturbed "perfect model" to a more realistic situation, in which the billiard can have noisy perturbations. These results generalize the ones obtained by Altmann and Endler[1]. Our idea is to reproduce and to extend the results of Ref. [1] to mixed phase space billiard systems, showing that the trapping of trajectories also exists in general billiards and thus can have consequences in physical devices. In particular, we would like to answer the following questions:

- Does noise also increase the trapping in open chaotic billiard systems?
- Can we quantify this trapping and relate it to the size of the phase space components?
- Can we fully characterize the survival probability in terms of phase space components?

One of the main difficulties of numerical analysis of transient chaos, in opposite to permanent chaos, is that most trajectories quickly (exponentially fast) exit the region of interest. Therefore it is computationally very expensive to perform the averages over long-living trajectories required to compute the main properties of these systems (e.g., the escape rate or the Lyapunov exponent in Eq. 1.9). This problem occurs because most of the current methods used to compute an average in an open dynamical system use an uniform distribution in the initial conditions.

The main idea we explore is to search for a more efficient sampling of initial conditions, which will still allow us to calculate the results we would have obtained had we sampled the phase space uniformly. One reason for this is that importance sampling techniques allow the use of phase space properties to improve the sampling. A more efficient sampling should be able to track more rare events which are exactly those that approach the chaotic saddle[17], and thus are the ones which better approach the statistical quantities of it. So, it is of utmost importance that an efficient sampling technique can be used on these systems[17, 30]. In particular, we would like to answer the following questions:

- Can we apply importance sampling techniques in phases-spaces with fractal structures? Is it worth it?
- Since we can think of $\rho(t)$ as a density of states, can we compute it using Landau algorithm[3]? Is it worth it?
- How are the phase space components of the dynamical system related with the properties of the sampling process? How can we take advantage of them?
- Is Monte Carlo integration worth in open dynamical systems?

While most of the computational topics were not included in this introduction, in Chap. 3 they will be properly introduced.

Chapter 2

Noise perturbed chaotic billiards

2.1 Characterization of the closed billiard

We now introduce a generic mixed phase-space billiard, the annular billiard. The annular billiard[31] is constructed from two circles, with radius' ratio r, and a distance between centers δ (see Fig 2.1(a)). We set $r = 0.3$, $\delta = 0.65$ because it depicts all the features of a typical chaotic billiard with mixed phase-space. This billiard constitutes a paradigmatic example of a chaotic billiard with mixed phase-space and we argue that our results are generic to mixed phase-space billiards.

We apply a section of surface on the condition $x^2+y^2 = 1$, like we have done in our toy model (Sec. 1.1.2)[31]. Along with the total energy conservation, this surface of section allows the 4-dimensional phase-space to be mapped to a two dimensional space with Birkoff coordinates $(\omega, \sin\alpha)$, defined in figure 2.1(a). On these coordinates, the particle's movement can be described by a two dimensional map[31]. This map considers two distinct possible behaviors between collisions: either the particle does not hit the inner circle, which we will call it the "a" map, or when it hits, which we will call the "b" map[31]. Notice that, by construction, it is not possible for the particle to hit the inner circle twice between two collisions with the outer circle. The map "a" can be written as

$$T_a\left(\omega_n, \alpha_n\right) : \begin{cases} \alpha_{n+1} & = \alpha_n \\ \omega_{n+1} & = (\pi - 2\alpha_n) \end{cases}$$

and the "b" as

$$T_b\left(\omega_n, \alpha_n\right) : \begin{cases} \alpha_{n+1} = \sin^{-1}\left(\sin\alpha_n + \delta\sin\left(\alpha_n - \omega_n\right) - \delta\sin\left(\phi_{n+1} + \beta_{n+1}\right)\right) \\ \omega_{n+1} = \phi_{n+1} + \beta_{n+1} - \alpha_{n+1} \end{cases}$$

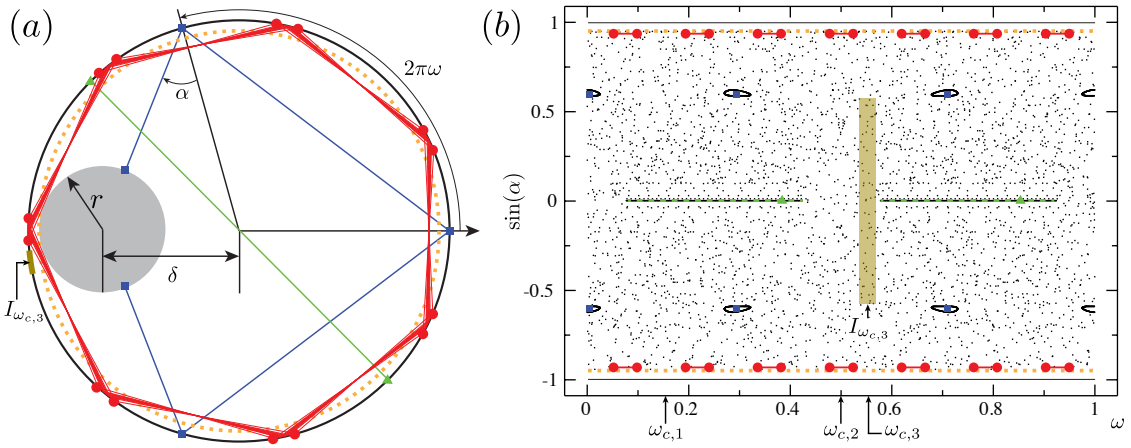

Figure 2.1: (Color online) The annular billiard with $r = 0.3$ and $\delta = 0.65$. (a) Configuration space showing selected periodic orbits. (b) Phase space obtained as a Poincaré surface of section at the outer circle. Shown MUPOs: $(2, 1)$ (green triangles), $(7, 1)$ (red circles) and KAM island around the period 6 orbit (blue squares). Black dots in (b) correspond to a single chaotic trajectory. Three positions of leaks are indicated: $\omega_{c,1} = 0.161$, $\omega_{c,2} = 0.5$, and $\omega_{c,3} = 0.55$ (the shaded region shows the leak $I_{\omega_{c,3}}$ used in Figs. 2.2 and 2.4).

where

$$\begin{cases} \beta_{n+1} & = \sin^{-1}\left(\frac{\sin\alpha_n + \delta\sin(\alpha_n - \omega_n)}{r}\right) \\ \phi_{n+1} & = \omega_n - \alpha_n + \beta_{n+1} \end{cases}$$

are the coordinates on the inner circle, needed to compute the new $(\omega_{n+1}, \sin\alpha_{n+1})$. The collision condition, which dictates which map to choose in each iteration, can be written as

$$h_c \equiv \left(\left|\sin\alpha_n + \delta\sin\left(\alpha_n - \omega_n\right)\right| \leq r\right) \ . \tag{2.1}$$

This way, the annular billiard is completely described by

$$\left(\omega_{n+1}, \alpha_{n+1}\right) = T\left(\omega_n, \alpha_n\right) = \begin{cases} T_b\left(\omega_n, \alpha_n\right) & \text{if } h_c \\ T_a\left(\omega_n, \alpha_n\right) & \text{else} \end{cases} \ .$$

Notice that if $\delta = 0$, $T_b = T_a$ and the map is the same as the toy model we have discussed in Chap. 1. So, the δ parameter can be seen as a perturbation to the unperturbed Hamiltonian, which, by KAM theorem, destroys its integrability.

The phase space in Birkhoff coordinates $(\omega, \sin\alpha)$ of the closed annular billiard is shown in 2.1(b). It can be divided in four invariant components 1-4, which are built by the trajectories that:

1. do not cross the inner circle of radius $r + \delta$ ($|\sin\alpha| \geq r + \delta$) and therefore never satisfy h_c in Eq. 2.1. Graphically they correspond to orbits close to the outer

boundary of the circle and it is called the *whispering gallery*. For the billiard used, the whispering gallery exists for $|\sin\alpha| < 0.95$, beyond the dotted line in Fig. 2.1. Notice that those orbits are described by the T_a, and thus this region is integrable, where the third constant of motion is the angle of incidence, α. The movement in this region is thus equivalent to our toy model.

2. cross the circle of radius $r + \delta$ ($\sin\alpha < r + \delta$) but never satisfy Eq. 2.1. These conditions are satisfied by periodic orbits that build one-parameter families of marginally unstable orbits (MUPOs). One trivial example is the diameter (period $p = 2$ and winding number $q = 1$ orbit) highlighted in Fig. 2.1 in green ▲. In opposite to the whispering gallery, these orbits are usually embedded in a chaotic component (see below) and affect the dynamics of chaotic trajectories despite having zero measure, see Ref. [16] for a detailed investigation in the annular billiard and Refs. [32, 33, 20] in other systems. For the billiard used, the following MUPOs (p, q) exist: $(2, 1)$, $(6, 1)$, $(7, 1)$, $(8, 1)$, $(9, 1)$, $(19, 2)$, $(29, 3)$, $(39, 4)$, $(49, 5)$, $(59, 6)$, $(69, 7)$, $(79, 8)$, $(89, 9)$,.... These MUPOs were calculated using the method described in Ref. [16].

3. cross the circle of radius $r + \delta$, satisfy the collision condition, but remain close to a stable periodic orbit. These orbits can be periodic, quasi-periodic, or even chaotic (confined inside the last quasi-periodic circle) and build the so-called Kolmogorov-Arnold-Moser (KAM) islands explained on the previous chapter. For the billiard used, the most prominent examples are the trajectories around the period 6 orbit shown as blue ■ in Fig. 2.1.

4. cross the circle of radius $r + \delta$ ($\sin\alpha < r + \delta$), satisfy h_c in Eq. 2.1, are chaotic, and fill a large component of the phase space. Despite the mathematical difficulties to provide rigorous proofs (see Refs. [34, 35] for rigorous results in particular cases), it is largely believed that the annular billiard with $\delta \gg 0$ contains a large chaotic component, in which a single trajectory visits a positive area of the phase space [31, 36, 29, 37]. This large component is called *chaotic sea* and, in the notation of the section 1.1.4.1, is responsible for the hyperbolic chaos. In Fig. 2.1(b) this region corresponds to the large dotted component.

2.2 Open billiard

2.2.1 Definition of the dynamics

We open the annular billiard by considering a region I at the border of the billiard through which the trajectories escape [38, 39, 40, 18, 28, 21, 20, 41]. Formally, the dynamics of the system with leak $\tilde{T}$ is defined based on the dynamics of the closed billiard T as:

$$\tilde{T}(\boldsymbol{r}) = \begin{cases} \text{escape} & \text{for } \boldsymbol{r} \in I \\ T(\boldsymbol{r}) & \text{else} \end{cases}$$

where $\boldsymbol{r} = (\omega, \sin\alpha)$. By convention, escape occurs only one time step after trajectories hit the leak, so that $\tilde{T}$ is defined in I. We are interested in finite but small I such that a non-trivial dynamics still exists in the billiard.

In the system discussed here, the chaotic saddle relevant to the escaping trajectories contains a hyperbolic component[22, 18]. However, as mentioned in Sec. 1.3.2, it also includes a non-hyperbolic component composed in this case by the borders of the whispering gallery [region 1 of Sec. 2.1], the MUPOs [region 2 of Sec. 2.1], and of the KAM islands [region 3 of Sec. 2.1].

In our simulations of the annular billiard we consider leaks $I = [\omega_c - \Delta\omega, \omega_c + \Delta\omega] \times [-\Delta\sin\alpha, +\Delta\sin\alpha]$ centered at three different positions ω_c (see Fig. 2.1), varying $\Delta\omega$, and a fixed $\Delta\sin\alpha = 2/3$. This configuration corresponds to a billiard where the leak is a dielectric material with refraction index $\eta = (\Delta\sin\alpha)^{-1} = 1.5$ (glass) with a perfect mirror boundary everywhere except inside the leak, where trajectories escape for collisions below the critical angle α_c with $\sin\alpha_c = 1/\eta$.

2.2.2 Survival probability $P(t)$

We compute the survival probability $P(t)$ inside the billiard by starting an ensemble of trajectories distributed according to an initial density $\rho_0(\boldsymbol{x})$. In our simulations we consider $\rho_0(\boldsymbol{x})$ to be uniform inside the leak of the billiard and 0 elsewhere. Physically, these initial conditions correspond to throwing trajectories inside the billiard through the leak. Another motivation for using this particular $\rho_0(\boldsymbol{x})$ comes from the fact that $P(t)$ in this case corresponds exactly to the distribution of Poincaré recurrence times [18]. The main decay regimes of $P(t)$ remain unaffected by this choice of $\rho_0(\boldsymbol{x})$, but the values of the exponents and transition times may change.

Figure 2.2 shows the decay of the survival probability for the particular leak shown in Fig. 2.1. We can identify three different regimes of decay [18, 19]

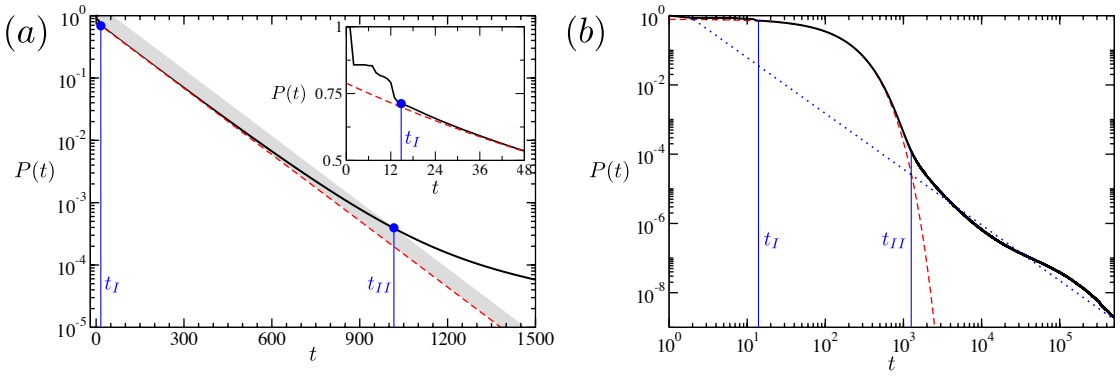

Figure 2.2: (Color online) The survival probability $P(t)$ for the open annular billiard. (a) Logarithmic scale in the y axis; Inset: x, y axes in linear scale, magnification for short times. (b) Logarithmic scale in both x, y axes. All regimes and transition times in Eq. 2.2 are depicted: the dashed line corresponds to the fitting of an exponential with $a = 0.72$ and $\gamma = 0.016$; and the dotted line corresponds to the fitting of a power law with $b = 2.492$ and $\beta = 1.65$. The transition times are $t_I = 14$ (visual inspection) and $t_{II} = 1020$. The leak is introduced in the position $\omega_{c,3}$ with $\mu(I) = 0.01$, see Fig. 2.1.

$$P_{deterministic}(t) \approx \begin{cases} irregular & \text{for } t < t_I \\ ae^{-\gamma t} & \text{for } t_I < t < t_{II} \\ bt^{-\beta'} & \text{for } t > t_{II}. \end{cases} \tag{2.2}$$

The dynamics of a typical trajectory escaping in each of the regimes in Eq. 2.2 can be associated to the phase space structures as:

- $t < t_I$ irregular: trajectories that collide only a few times in the chaotic sea of the closed billiard [region 4 of Sec. 2.1], the spatial density of survival trajectories has not converged yet. The exact shape in this regime is extremely sensitive to $\rho_0(\boldsymbol{x})$[18].

- $t_I < t < t_{II}$ exponential $e^{-\gamma t}$: trajectories explore the hyperbolic component of the chaotic saddle but escape before coming close to the border of the non-hyperbolic components [items (1,2,3) of Sec. 2.1]. Analogous to the case of fully chaotic systems [17], the same exponent γ is observed for different $\rho_0(\boldsymbol{x})$ [18].

- $t > t_{II}$ power-law $t^{-\beta'}$: trajectories get stuck close to the non-hyperbolic components of the saddle due to stickiness (See Sec. 1.2.1). The asymptotic exponent changes from β' to $\beta'' = \beta' - 1$ for $\rho_0(\boldsymbol{x})$ nonzero at the boundary of the

non-hyperbolic components (e.g., if $\rho_0(\boldsymbol{x})$ is taken according to the Liouville measure restricted to the chaotic sea of the closed billiard) [10, 17].

The description above applies to typical trajectories escaping in the corresponding regimes. It is instructive to think that for intermediate times, $t_\beta < t < t_{II}$, both exponential and power-law regimes coexist [18, 32, 21]

$$P(t) = ae^{-\gamma t} + bt^{-\beta'} \tag{2.3}$$

where t_{II} is the time needed to approach the non-hyperbolic component of the saddle [18].

2.2.3 Dependence of the parameters of $P(t)$ on the leak

As we have seen in the Chap. 1, the **exponential decay** γ in 2.2 can be considered a signature of the chaoticity of the map. Following this reasoning, for small leaks we can approximate the escape at each time step by the area of the leak relative to the area of the chaotic sea $\mu(I) = \text{Area}(I)/\text{Area(chaotic sea)}$. For the billiard considered here we found numerically that Area(chaotic sea) $\approx 0.993 \times (r + \delta) = 0.943$. Using phase-space areas correspond to using the Liouville measure $d\mu = d\omega d\sin\alpha$ of the closed system to approximate properties of the open system, and can be shown to be valid for almost all leak positions in strongly chaotic systems [41]. This leads to an estimation of the exponential decay as

$$\gamma^* = -\ln(1 - \mu(I)) \approx \mu(I) \text{ for } \mu(I) \to 0. \tag{2.4}$$

Violations of this approximation in the fully chaotic case have been extensively discussed in the recent years and are particularly large for leaks containing low-period periodic orbits of the closed system[39, 18, 40]. Here we extend these previous results and verify the effectiveness of the approximation in Eq. 2.4 for the intermediate-time exponential decay in Eq. 2.2. In Fig. 2.3(a) we compare the numerically obtained values to the prediction for different leak sizes centered at three different positions: in the chaotic region, around an unstable periodic orbit, and around a family of MUPOs. In all cases $\gamma \to \gamma^*$ is observed in the limit of small leaks $\mu(I) \to 0$, in agreement with relation2.4. For large leak sizes, Fig. 2.3(a) shows different deviations of this relation, in agreement with the results observed for hyperbolic systems[39, 18, 40].

The importance of the value of γ is mentioned in Sec. 1.3. Besides, the same value of γ is obtained for a broad class of smooth initial densities ρ_0. In fully chaotic systems the requirement is that ρ_0 intersects the stable manifold of the chaotic saddle.

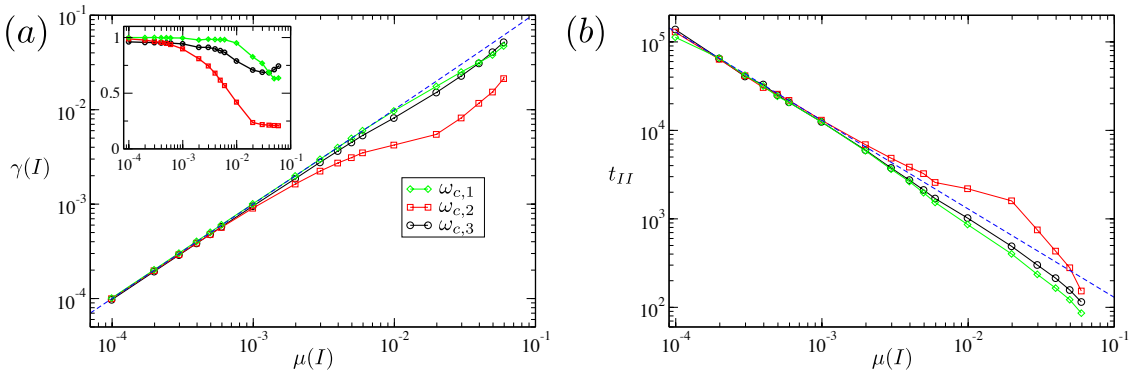

Figure 2.3: (Color online) Scalings of the parameters of $P(t)$ in Eq. 2.2 with leak size $\mu(I)$ for three different leak locations. (a) Intermediate times escape rate γ; The dashed line corresponds to γ^* in Eq. 2.4. Inset: dependence of the coefficient a with $\mu(I)$. (b) Transition time t_{II}, obtained using Eq. 2.5; the dashed line corresponds to a scaling $1/\mu(I)$. The leaks have a fixed height $\Delta \sin\alpha = 2/3$ and varying width $\Delta\omega \to 0$, which leads to $\mu(I) \to 0$. The centers of the leaks are: $\omega_{c,1} = 0.161$ (in a MUPO, black circles), $\omega_{c,2} = 0.5$ (in an unstable periodic orbit, red squares), and $\omega_{c,3} = 0.55$ (in the chaotic sea, green diamonds).

Analogously, the requirement here is that it intersects the stable manifold of the hyperbolic component of the chaotic saddle.

The **power-law exponent** β' depends on the properties (of the boundary) of the non-hyperbolic sets embedded in the chaotic component of the phase space (components 1, 2 and 3 in the list of Sec. 2.1) and the dependences were presented in Sec. 1.2.1 and Sec. 1.2.1.

2.2.4 Dependence of the transition times of $P(t)$ on the leak

Transition time t_I indicates the starting of the exponential decay. It can be interpreted as a convergence time which is proportional to $1/|\lambda'|$, where λ' is the negative Lyapunov exponent of the saddle (the time to relax to the hyperbolic component of the saddle along its stable manifold). Numerical observations usually show an abrupt approach, i.e., the exponential decay provides a good description of $P(t)$ after a finite (short) time[18].

The transition time t_{II} is defined from Eq. 2.3 as the time for which the exponential and power-law contributions are equal[18]

$$ae^{-\gamma t_{II}} = bt_{II}^{-\beta'} \Rightarrow p(t_{II}) = 2\gamma a e^{-\gamma t_{II}}. \tag{2.5}$$

The ratio a/b can be interpreted as the proportion between the number of trajectories escaping exponentially to the number of trajectories escaping algebraically. It depends mainly on the measures of the chaotic and regular components of the phase space and therefore it should not depend strongly on the measure of the leak $\mu(I)$. Under this assumption we can estimate the scaling of t_{II} on the leak size $\mu(I)$ as[18]

$$t_{II} \sim \frac{1}{\gamma} \sim \frac{1}{\mu(I)}, \tag{2.6}$$

for which additional logarithmic corrections apply[32]. The scaling in Eq. 2.6 has been confirmed in our numerical simulations for the three different leak positions, see Fig. 2.3(b).

2.3 Open noisy billiard

2.3.1 Definition of the dynamics

Here we consider additive noise perturbations to the trajectories. In the simulations of the annular billiard we have implemented at each collision a perturbation to the angle α as

$$\alpha' = \alpha + \delta,$$

where δ is an independent normal distributed random variable with zero mean, $\langle\delta\rangle = 0$, and standard deviation $\sigma_\delta = \pi\xi$ (noise strength). In order to prevent the particle from leaving the billiard through the border (non-physical situation), the noise distribution was truncated at $\alpha = \pm\pi/2$. Notice that perturbations in the α direction are perpendicular to the border of the whispering gallery component and to the parameterization of the billiard boundary, having therefore a strong impact on sliding orbits $\alpha = \pm\pi/2$[1]. Based on previous observations with different setups[42, 1, 43, 44], and in the generality of the arguments below, we believe our results are valid for additive white noise in general (provided the perturbation in α is nonzero). It is an interesting open question whether (and which) modifications are needed for multiplicative and colored noise (see Ref. [45]).

[1]In fact, trajectories have a tendency of being repelled from sliding orbits because the noise perturbation in α is nonzero, truncated in $\alpha = \pm\pi/2$, and added on each collision. Therefore, we do not expect these orbits to dramatically affect $P(t)$ or the relation between billiard maps and flows in our case.

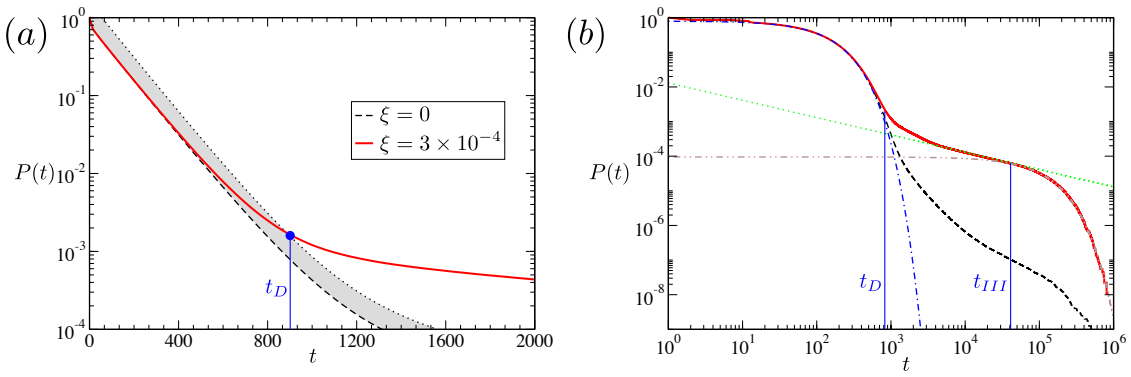

Figure 2.4: (Color online) Survival probability $P(t)$ for the open annular billiard perturbed by noise with intensity $\xi = 3 \times 10^{-4}$. (a) Logarithmic scale in the y axis; (b) Logarithmic scale in both x and y axis. All regimes and transition times in Eqs. 2.7-2.8 are depicted in (b): fitting of the asymptotic exponential with $d = 9.34 \times 10^{-5}$ and $\gamma_\xi = 1.06 \times 10^{-5}$ (dot-dashed line in brown); power-law decay with $c = 0.014$ and $\beta_{RW} = 0.5$ (dotted line in green). The dashed black line corresponds to the $\xi = 0$ case (see Fig. 2.2). The transition times were estimated as $t_D = 887$ and $t_{III} = 15,158$. The leak is as in Fig. 2.2 ($\omega_{c,3}$ with $\mu(I) = 0.01$).

2.3.2 Survival probability $P(t)$

In Sec. 2.2.2 the trapping of trajectories inside the billiard was connected to invariant structures of the deterministic phase space. The longer the escape time of trajectories, the closer they approach these invariant structures. This leads to a connection between temporal scales of the survival probability and spatial scales in the phase space. Noise perturbations affect phase-space scales comparable to ξ. Based on these arguments we expect that for small ξ the survival probability $P(t)$ is modified for long times only:

$$P(t) \approx \begin{cases} P_{\text{deterministic}} & \text{for } t < t_D, \\ P_{\text{noise}} & \text{for } t > t_D, \end{cases} \tag{2.7}$$

where $P_{\text{deterministic}}$ is given by Eq. 2.2 and t_D is the transition time. Following Refs. [42, 1], the noise perturbed survival probability is given by

$$P_{\text{noise}}(t) \approx \begin{cases} ct^{-\beta_{RW}} & \text{for } t_D < t < t_{III}, \\ de^{-\gamma_\xi t} & \text{for } t > t_{III}. \end{cases} \tag{2.8}$$

Figure 2.4 shows, for $\xi = 3 \times 10^{-4}$, the different decay regimes and transition times of the survival probability given by Eqs. (2.7-2.8). The dynamics of a typical

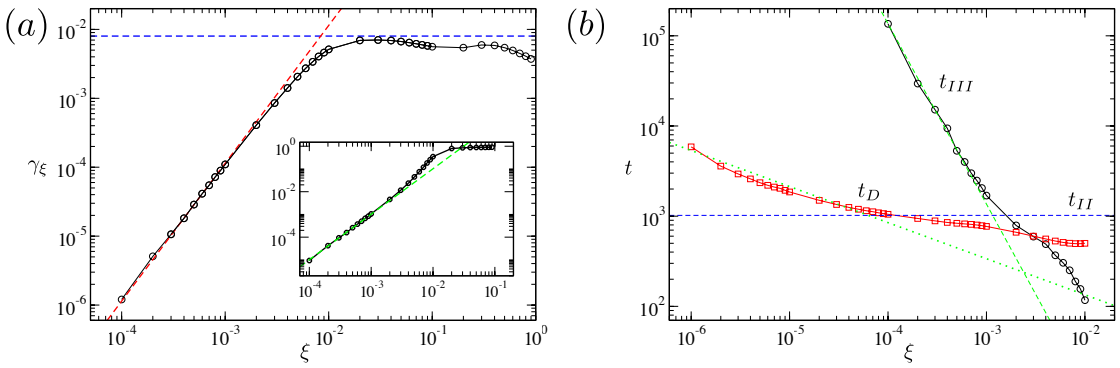

Figure 2.5: (Color online) Dependence of the parameters of $P(t)$ in Eq. 2.8 with noise intensity ξ. (a) Fitted γ_ξ with scaling ξ^2 (red dashed line) and value γ (blue dots). Inset: coefficient d vs. ξ with green dashed line representing ξ^{-2}; (b) t_{III} obtained as the time for which $P(t)$ intersects the fitted curve $1.1d\exp(-\gamma_\xi t_{III})$ (black circles); t_D obtained as the time for which $P(t)$ intersects $2P_{\text{deterministic}}(t)$ (red squares); and green dotted lines indicating scalings $\xi^{-0.4}$ (bottom) and ξ^{-2} (top). The leak is the same as in Figs. 2.2 and 2.4.

trajectory escaping in each of these regimes can be associated to the phase space structures of the deterministic dynamics as:

- $t < t_D$ deterministic: trajectories escape before the noise perturbation is noticed, $P(t)$ coincides with the $\xi = 0$ case.
- $t_D < t < t_{III}$ enhanced trapping: trajectories enter the region corresponding to regular motion of the deterministic dynamics [components 1 and 3 of Sec. 2.1] and perform a one-dimensional random walk inside it[42, 44, 1, 43, 46].
- $t > t_{III}$ asymptotic exponential: trajectories explored all available phase-space.

In this description we neglect the effect of noise on γ, which has been investigated for a fully chaotic system in Ref. [1]. The sticky region around MUPOs [region 2 of Sec. 2.1] does not contribute to the enhanced trapping regime ($t_D < t < t_{III}$) because MUPOs build a zero measure set. This means that if noise is added to a system in which MUPOs are the only source of stickiness (e.g., the Stadium[21] or Drive-belt billiards [20]), we predict that the exponential decay will start immediately after t_D (i.e., $t_{III} = t_D$).

2.3.3 Dependence of the parameters of $P(t)$ on the leak

For small noise perturbations the parameter β_{RW} in Eq. 2.8 can be related to the scaling of the recurrence time distribution of a one-dimensional random walk (with step size $\sim \xi$) and is therefore given by [47, 42]

$$\beta_{RW} = \frac{1}{2} \text{ for } \xi \to 0. \tag{2.9}$$

In the derivation of this result in Ref. [42] (see also [1]) the initial conditions $\rho_0(\boldsymbol{x})$ were chosen *outside* KAM islands of the deterministic closed billiard, in agreement with the case treated here. See Refs.[44, 43, 46] for the case of $\rho_0(\boldsymbol{x})$ *inside* KAM islands. References [43, 46] also showed that if ξ^2 terms are included, the random walk is biased.

The scaling in Eq. 2.9 is interrupted for long times because of the limited region available for the random walk in the KAM islands and whispering gallery. In the random-walk model this corresponds to adding a reflecting boundary condition [42, 1]. The exponent γ_ξ of the asymptotic decay can be obtained considering $P(t)$ to be a continuous and smooth function around $t = t_{III}$. Evaluating

$$\frac{\partial \log(P(t))}{\partial t} \text{ at } t = t_{III} \tag{2.10}$$

for both terms in Eq. 2.8 and equating then leads to $t_{III} = 0.5/\gamma_\xi$. Below we show that $t_{III} \sim 1/\xi^2$ [see Eq. 2.13 and Refs. [42, 1]], and therefore we obtain

$$\gamma_\xi \sim \frac{1}{t_{III}} \sim \xi^2 \text{ for } \xi \to 0. \tag{2.11}$$

This scaling is confirmed in Fig. 2.5(a). Interestingly, we observe that for larger noise intensities γ_ξ experiences a crossover to $\gamma_\xi \approx \gamma$, i.e., γ_ξ is bounded by the escape rate observed for short times which was related to the hyperbolic component of the chaotic saddle in Sec. 2.1. This observation indicates that once the trajectories leave the region corresponding to regular motion of the deterministic dynamics, the hyperbolic component of the saddle controls their escape. For small noise the process of leaving the regular components is slower and therefore the scaling of Eq. 2.11 dominates γ_ξ. For larger noise, the deterministic exponential escape is slower than the escape from the islands and therefore $\gamma_\xi \approx \gamma$ is observed. In Ref. [44] a similar but different scaling of γ_ξ on ξ was numerically obtained for the case of random maps and for initial conditions taken inside the KAM islands.

2.3.4 Dependence of the transition times of $P(t)$ on the leak

A theory for t_D can be found in Ref. [48] and predicts that

$$t_D \sim 1/t^{\Lambda} \text{ for } \xi \to 0, \tag{2.12}$$

with $\Lambda \lessapprox 1$ related to the scaling of the *Cantori* close to the KAM islands. This scaling is valid for $t_D \gg t_{II}$ because for $t_D \simeq t_{II}$ the deterministic trapping around the KAM islands has a limited contribution.

The final cut-off time t_{III} can be estimated from basic properties of diffusion motion. The expected distance L traveled by a random walker with step-size $\sim \xi$ grows as $L \sim \xi\sqrt{t}$. The time t_{III} corresponds to the expected time for the ξ-perturbed trajectories to travel the (fixed) distance corresponding to the diameter of the (largest) KAM island. Therefore, we estimate

$$t_{III} \sim \xi^2, \text{ for } \xi \to 0. \tag{2.13}$$

Our numerical simulations for the scaling of the transition times are shown in Fig. 2.5(b). We see that for times comparable to t_{II} only a weak dependence of t_D on ξ is observed. For times larger than t_{II} our results indicate an increase of this dependency, consistent with relation 2.12. The scaling of t_{III} in Eq. 2.13 is confirmed over a larger interval of ξ.

Chapter 3

Sampling on dynamical systems' phase-space

We now turn to the second problem of the thesis, as explained in Sec. 1.4, Our goal is to develop a new approach to compute the escape time distribution, using a non-uniform sampling.

3.1 Statistical physics approach

Let T be a discrete map, Ω its phase space or some relevant part of it, $\boldsymbol{r} \in \Omega$, and I a leak on the system such that we can define

$$\begin{aligned} t_e(\boldsymbol{r}): \ \Omega &\rightarrow \mathbb{N} \\ \boldsymbol{r} &\rightarrow t_e(\boldsymbol{r}) \end{aligned}$$

as the time (number of iterations) a trajectory with initial condition $\boldsymbol{r}$ leaves the system by the leak, which we call the *escape time*. With this definition, the map and the leak are encapsulated in $t_e(\boldsymbol{r})$: to calculate $t_e(\boldsymbol{r})$ from $\boldsymbol{r}$, we iterate forward in time the map until it fulfills the escape condition of leaving from the leak. The escape time distribution defined in chapter 1 can then be written as an average over Ω,

$$\rho(t) = \frac{1}{V} \int_{\Omega} \delta_{t,t_e(\boldsymbol{r})} d\boldsymbol{r} \tag{3.1}$$

where $\delta_{i,j}$ is the delta Kronecker and

$$V = \int_{\Omega} d\boldsymbol{r}$$

is the phase-space volume.

To estimate any mean value, $\langle Q \rangle$, the general approach is to pick N random initial conditions $\boldsymbol{r}_i$, with $t_i = t_e(\boldsymbol{r}_i)$, from an arbitrary probability distribution $p(\boldsymbol{r})$ defined on Ω, which we call the *sampling distribution*, and use the estimator[49]

$$Q_N = \frac{1}{Z} \sum_{i=1}^{N} p^{-1}(\boldsymbol{r}_i) Q(\boldsymbol{r}_i) \tag{3.2}$$

where

$$Z = \sum_{i=1}^{N} p^{-1}(\boldsymbol{r}_i) \ .$$

This estimator converges to the true value of $\langle Q \rangle$ by the law of large numbers, which is the main result of *importance sampling*. When we sample states uniformly in the phase-space, $p(\boldsymbol{r}) = 1/V$, we obtain, from Eq. 3.2

$$Q_N = \frac{1}{N} \sum_{i=1}^{N} Q(\boldsymbol{r}_i)$$

which is the usual estimator used. If we want to compute $\rho(t)$ using an arbitrary distribution $p(\boldsymbol{r})$, we can use the estimator

$$\rho(t)_N = \frac{1}{Z} \sum_{i=1}^{N} p^{-1}(\boldsymbol{r}_i) \delta_{t,t_e(\boldsymbol{r}_i)} \ . \tag{3.3}$$

We have seen in Sec. 1.3 that the quantity $\delta_{t,t_e(\boldsymbol{r})}$ can be non-trivial: it can be fractal-like. Our initial question is if there is any $p(\boldsymbol{r})$ that can help to improve our sampling? The answer is not clear in general problems. For instance, when the uniform distribution is used, we have that

$$\rho(t)_N = \frac{1}{N} \sum_{i=1}^{N} \delta_{t,t_e(\boldsymbol{r}_i)}$$

but from Eq. 1.11, in open hyperbolic systems the probability to sample states with high escape times decays exponentially. This means that the numerical efford needed in the estimation of $\rho(t)$ will exponentially increase with t. This is valid for any quantity that depends on the escape time, $Q(t_e(\boldsymbol{r}))$.

Our idea is to use the phase-space structure of dynamical systems, introduced in Chap. 1, to implement an efficient sampling technique. From the practical point of view, importance sampling requires states to be sampled according to the arbitrary distribution $p(\boldsymbol{r})$.

3.2 Metropolis Algorithm

A common solution to generate states $\boldsymbol{r}$ according to an arbitrary distribution $p(\boldsymbol{r})$ is the *Metropolis algorithm*[50, 49]. Metropolis algorithm uses a discrete time markovian stochastic process, also called a *Markov chain*[1]. In a Markov chain, each step only depends on the present state (in this case, one point $\boldsymbol{r}$ on the phase-space) and the step consists in generating another state, $\boldsymbol{r}'$. The quantity of interest in each step is the transition probability, $P(\boldsymbol{r} \to \boldsymbol{r}')$, which is the conditional probability of transiting to a new state $\boldsymbol{r}'$ given the present state $\boldsymbol{r}$. By probability conservation in every step the system must transit from its state to some state of the phase space, i.e.

$$\int_{\Omega} P(\boldsymbol{r} \to \boldsymbol{r}')\, d\boldsymbol{r}' = 1 \ .$$

Notice that there is a non-zero probability of the system staying in the same state after one step, i.e. $P(\boldsymbol{r} \to \boldsymbol{r})$ can be different from zero.

The Metropolis algorithm resides in conditioning $P(\boldsymbol{r} \to \boldsymbol{r}')$ such that the Markov chain generates states according to the probability distribution $p(\boldsymbol{r})$. To this end, it employs two conditions on the Markov chain: *ergodicity* and *detailed balance*:

Ergodicity

In a Markov process, ergocity of the Markov chain is obtained by forcing it to have non-zero transition probability from any $\boldsymbol{r} \in \Omega$ to any other $\boldsymbol{r}' \in \Omega$ in a finite number of steps (not necessarily in each single step). I.e. all states must be accessible. Ergodicity ensures that there is at most one asymptotic distribution[51].

Detailed Balance

Detailed balance states that the probability of the system to be in $\boldsymbol{r}'$ and transit to $\boldsymbol{r}$ must be equal to the probability of the system to be in $\boldsymbol{r}$ and transits to $\boldsymbol{r}'$ *in each Markov step*. It ensures that the asymptotic distribution exists and is $p(\boldsymbol{r})$[51]. Formally, if $p(\boldsymbol{r})$ is the probability we want to sample from, the Markov process is detailed balanced if $P(\boldsymbol{r} \to \boldsymbol{r}')$ fulfills

$$P(\boldsymbol{r} \to \boldsymbol{r}')\, p(\boldsymbol{r}) = P(\boldsymbol{r}' \to \boldsymbol{r})\, p(\boldsymbol{r}') \ \ \forall \boldsymbol{r}, \boldsymbol{r}' \ . \tag{3.4}$$

[1]For practical purposes, we will say that each discrete time step of the chain will be called a "step", to avoid confusion with the escape time.

This condition ensures that a Markov process will, for sufficient long times, generate states according to $p(\boldsymbol{r})$ (see Ref. [49]). One valid question is what $P(\boldsymbol{r} \to \boldsymbol{r}')$ fulfills Eq. 3.4. Considering that we have specified $p(\boldsymbol{r}) \neq 0$, Eq. 3.4 can be written as

$$\frac{P(\boldsymbol{r} \to \boldsymbol{r}')}{P(\boldsymbol{r}' \to \boldsymbol{r})} = \frac{p(\boldsymbol{r}')}{p(\boldsymbol{r})} \ . \tag{3.5}$$

However, the choice of $P(\boldsymbol{r} \to \boldsymbol{r}')$ that satisfies this condition is not unique. One common solution is to express $P(\boldsymbol{r} \to \boldsymbol{r}')$ as

$$P(\boldsymbol{r} \to \boldsymbol{r}') = g(\boldsymbol{r} \to \boldsymbol{r}')\, A(\boldsymbol{r} \to \boldsymbol{r}')$$

where we call $g(\boldsymbol{r} \to \boldsymbol{r}')$ the *proposal probability* and $A(\boldsymbol{r} \to \boldsymbol{r}')$ the *acceptance probability*. The proposal probability is the probability of picking (propose) a new state $\boldsymbol{r}'$, given that we are at $\boldsymbol{r}$. The acceptance probability is the probability of accepting that proposal. So, a typical implementation of the Markov step consists in two sub-steps: the proposal, which chooses the $\boldsymbol{r}'$ state according to $g(\boldsymbol{r} \to \boldsymbol{r}')$, and an acceptance, which decides if the system transits or not to $\boldsymbol{r}'$ according to $A(\boldsymbol{r} \to \boldsymbol{r}')$. Because the choice of $P(\boldsymbol{r} \to \boldsymbol{r}')$ is arbitrary, given that it fulfills Eq. 3.5, Metropolis proposed a choice that fulfills Eq. 3.5, called the *Metropolis choice*[49]:

$$A(\boldsymbol{r} \to \boldsymbol{r}') = \min\left(1, \frac{g(\boldsymbol{r}' \to \boldsymbol{r})\, p(\boldsymbol{r}')}{g(\boldsymbol{r} \to \boldsymbol{r}')\, p(\boldsymbol{r})}\right) \tag{3.6}$$

This choice is now widely used and its main motivation is that, for the case $g(\boldsymbol{r}' \to \boldsymbol{r}) = g(\boldsymbol{r} \to \boldsymbol{r}')$ (e.g. a random uniform selection), if we would like the system to be more likely in $\boldsymbol{r}'$ than in $\boldsymbol{r}$, $p(\boldsymbol{r}') > p(\boldsymbol{r})$, then we automatically accept the transition; otherwise, we accept with probability $p(\boldsymbol{r}')/p(\boldsymbol{r}) < 1$. An important example that connects with statistical physics[2] is $p(\boldsymbol{r}) \propto \exp(\beta t_e(\boldsymbol{r}))$ and g such that $g(\boldsymbol{r}' \to \boldsymbol{r}) = g(\boldsymbol{r} \to \boldsymbol{r}')$. In this case

$$A(\boldsymbol{r} \to \boldsymbol{r}') = \min\left[1, e^{\beta(t_e(\boldsymbol{r}') - t_e(\boldsymbol{r}))}\right] \ .$$

This choice is normally used in statistical physics for sampling states on a system in contact with an heat bath, and is known as the Metropolis-Hastings algorithm (with the respective adaptation that the $-t$ here plays the role of energy). Its motivation is related to the Boltzmann distribution, as Metropolis pointed out:

[2]The perfect analogy to the physical Metropolis-Hastings algorithm would have a minus sign. In physics, the states with higher weight are the ones with low energy. Here we would be interested in giving more contribution to states with high escapes time, which are the ones with lower number of states.

> *Instead of choosing configurations randomly, then weighting them with* $\exp(-E/kT)$*, we choose configurations with a probability* $\exp(-E/kT)$ *and weight them evenly.*
>
> — Metropolis et al., [52].

3.3 Multicanonic and Landau Algorithm

3.3.1 Multicanonic choice

One pertinent pathology of the Metropolis-Hastings algorithm is that the simulation normally gets stuck in regions with high escape times[51]. This happens because the probability to jump from one region to other goes exponentially, as $\exp(\beta\Delta t) \sim 0$ if $\Delta t \gg 1$ is the time difference between those regions[51]. The consequence is that states with equal escape times are not equally sampled, contradicting the method's assumption, thus biasing it and effectively causing $\boldsymbol{r}$ not to be sampled according with $p(\boldsymbol{r})$. To avoid this pathology, Berg and Neuhaus[53] proposed a choice of $p(\boldsymbol{r})$, named *multicanonic* (also called entropic or flat histogram) choice which considers sampling $\boldsymbol{r}$ according to the inverse of the density of states:

$$p(\boldsymbol{r}) = \frac{1}{\rho(t_e(\boldsymbol{r}))} \equiv e^{-S(t_e(\boldsymbol{r}))} \tag{3.7}$$

where S is called the entropy (logarithmic of the density of states). With this choice, the probability to sample a time t is

$$\frac{1}{V}\int_{\Omega} p(\boldsymbol{r})\,\delta_{t,t_e(\boldsymbol{r})}d\boldsymbol{r} = \frac{1}{t_{max}-t_{min}} = \text{const} \tag{3.8}$$

i.e. all times are equally sampled (and thus the name flat histogram). The main motivation for this choice is that the Δt barriers are no longer difficult to overcome. More importantly, *the error bars of the measured quantities are constant for all times* because each time is equally sampled. Compared to the Metropolis paradigm, this choice can be thought as

> Instead of choosing random states uniformly, we choose random escape times uniformly.

One important question in this approach is that we generally do not know $\rho(t)$ *a priori*: in fact, we would like to compute it. So, a multicanonic simulation could only work after we knew $\rho(t)$, which we would have to compute using other sampling technique.

3.3.2 Landau algorithm

In 2001, Wang and Landau[3] proposed an algorithm which calculates the density of states of a system. Our idea is to generalize the algorithm to dynamical systems by taking into account that $\rho(t)$ resembles a density of states. Landau algorithm uses a non-markovian approach which converges to the Markov multicanonic algorithm. The adaptation of the Landau algorithm to this case is the following: we set $S(t) = 0\ \forall t$ and $f = 1$. Next, we iterate the system using a Markov step and propose a given $\boldsymbol{r}'$ according to $g(\boldsymbol{r} \to \boldsymbol{r}')$. We accept/reject it according to Eq. 3.6 and every time the system is at t, we increase the entropy of that escape time by a constant factor,

$$S(t) \leftarrow S(t) + f\ . \tag{3.9}$$

Because the probability to accept a transition to time t decreases with increasing $S(t)$ (see Eq. 3.6), it is now less probable to find the system with an escape time t already visited. This procedure leads to a flat histogram in the variable t[3], which means that the entropy is built (using Eq. 3.9) as an approximation of the "exact" entropy, with an error of the order of $\sqrt{f}$[54, 55]. Taking $f \leftarrow f/2$ and repeating the process, this error will decrease because the process keeps making the histogram constant. In the limit of $f \to 0$, S will be approximating the exact entropy because that is the requirement to a flat histogram, which is being kept. The important point is that since the histogram is constant, Eq. 3.8 holds, which means, from Eq. 3.7, that the process is sampling according to $\rho(t)$. It can be shown that the final error of S will be related on both how f is updated and its final value (see Ref. [54, 55] on the convergence of Landau algorithm).

It is important to mention that Landau algorithm performs a random walk in the initial conditions of the phase-space: we pick an initial state $\boldsymbol{r}$, and we have a probability $P(\boldsymbol{r} \to \boldsymbol{r}')$ to jump to another state $\boldsymbol{r}'$. However, Landau algorithm does not use a Markov process: the probabilities $P(\boldsymbol{r} \to \boldsymbol{r}')$ are changing, since S is changing during the simulation. In the limit $f \to 0$, $S(t)$ converges to a constant quantity and thus $P(\boldsymbol{r} \to \boldsymbol{r}')$ is also constant. On that limit we are in a Markov process.

3.3.3 Implementation of Landau algorithm

We now provide an illustrative example showing how can the Landau algorithm be implemented to compute the escape time distribution of a dynamical system. We

consider the update given by Eq. 3.9, and a proposal given by a Gaussian distribution centered in $\boldsymbol{r}$,

$$g\left(\boldsymbol{r} \to \boldsymbol{r}'\right) = \frac{1}{\sqrt{2\pi\sigma^2}} \exp\left(-\frac{\left|\boldsymbol{r} - \boldsymbol{r}'\right|^2}{2\sigma^2}\right) \ , \tag{3.10}$$

with the *anzatz* motivated by the typical scalings found on hyperbolic systems

$$\sigma = \sigma\left(t\right) = b \exp\left(-\lambda t\right) \ ,$$

where b, λ are, for now, arbitrary constants and $t = t_e\left(\boldsymbol{r}\right)$. This choice leads to

$$\frac{g\left(\boldsymbol{r}' \to \boldsymbol{r}\right)}{g\left(\boldsymbol{r} \to \boldsymbol{r}'\right)} = \frac{\sigma}{\sigma'} \exp\left(-\frac{\mu^2}{2}\left(\frac{1}{\sigma'^2} - \frac{1}{\sigma^2}\right)\right)$$

which will be needed to compute the acceptance. Notice that $g\left(\boldsymbol{r} \to \boldsymbol{r}'\right)$ could be any distribution as long as the Markov matrix fulfills detailed balance (Eq. 3.4). The first reason for this choice is that it makes the Markov chain fullfils ergodicity: because each step allows the proposal of any state in the phase-space, the Markov chain is ergodic and we fulfill the ergodic condition required by the algorithm. The second reason is less trivial: the idea is that we would like to ensure *locality*. We say that the dynamics is local if the steps are small when compared with the size of the spectra:

$$\left|\Delta t\right| \equiv \left|t_e\left(\boldsymbol{r}'\right) - t_e\left(\boldsymbol{r}\right)\right| \ll t_{max} - t_{min} \tag{3.11}$$

The reason for requiring locality is to ensure that we perform local steps in the escape time. The advantage of local steps in the escape time is that we can control the random walk in the escape time variable and thus help the importance sampling to sample all the spectra. A Gaussian distribution is a distribution in which a parameter has units of distance and depends on the escape time of the state the system is in, $\boldsymbol{r}$. The relationship between Δt and ε is now encapsulated in the choice of $\sigma\left(t\right)$, with which we will deal later.

With the previous definitions, the Landau algorithm can be described by the following steps:

1. **Initialization**: make all entries of the entropy S within $[t_{min}, t_{max}]$ equal to zero and set $f = 1$; pick an initial state $\boldsymbol{r}$ at random and calculate its escape time, $t = t_e\left(\boldsymbol{r}\right)$.

2. **Markov chain**:

   (a) Proposal: pick a random $\boldsymbol{r}'$ according to Eq. 3.10 and calculate $t' = t_e\left(\boldsymbol{r}'\right)$.

(b) Acceptance: generate a pseudo-random number $z \in [0, 1]$. If $z < A(\boldsymbol{r} \to \boldsymbol{r}')$ from Eq. 3.6, accept the choice, thus setting $\boldsymbol{r} \leftarrow \boldsymbol{r}'$ and $t \leftarrow t'$; if not, do nothing.

(c) S-update: make $S(t) \leftarrow S(t) + f$;

(d) Repeat M times.

3. **Entropy convergence/Landau step**: make $f \to f/2$; repeat 2. and 3 until $f < f_{min}$.

4. **Finalization**: with the $S(t)$, calculate $\rho(t) = e^{S(t)}$.

One undefined parameter of this implementation is the value of M: if M is too low, we would not be able to ensure that all the phase-space is visited. Of course "too low" is difficult to tell on a general system. This reason motivates the use of other control parameter, the *tunneling time*[51, 56, 57]. One tunneling time is defined as the number of steps needed to perform a round-trip between the minimum escape time and the maximum escape time. The motivation to use tunneling times is that we are not interested in how many steps are performed, but how the simulation is moving throughout the spectrum. Given one round-trip, we ensure that we have been in both $t = t_{max}$ and $t = t_{min}$. If we set $\sigma(t_{min})$ of the order of the phase-space's maximum distance, we ensure that, at least once, every state in the phase space is proposed at each f. So, in our implementation, we choose to perform M round-trips at each f.

3.3.4 Proof of concept

To confirm that the Landau algorithm can be applied to a generic open chaotic system, we apply the method, described in the previous section, to the hyperbolic Hénon map, defined in Sec. 1.3 with $k = 6$. By manually varying λ, we have obtained $\lambda \simeq 1.31$, $b = 1$ as good parameters in Eq. 3.10 for a reasonable fast round trip. In figure 3.1 we show both the histogram of proposals and the histogram of the visited places as a function of the initial conditions, $I_{initial}$ (compare with Fig. 1.7b). Because our algorithm samples more states with higher times than in uniform sampling, states near the stable manifold's crossing are more often picked. The result, is a significant gain in efficiency, as is clearly shown in Fig. 3.2. It shows that not only a better estimation is accomplished with the same number of map iterations (which are of $O(1)$ and thus comparable with computational effort), but we can also sample states with much

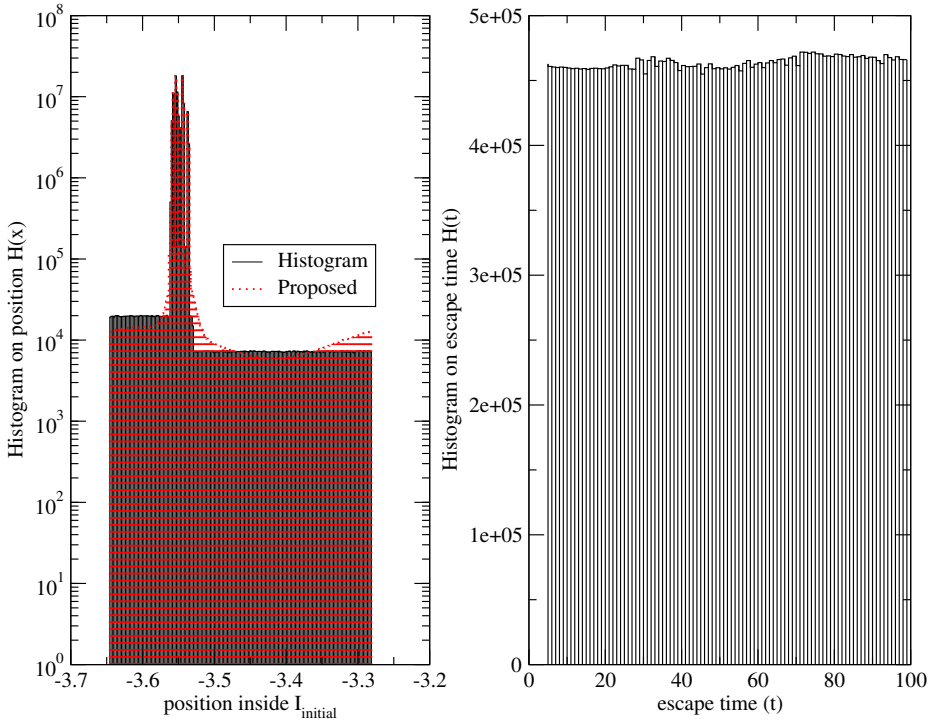

Figure 3.1: Histograms of the Landau algorithm on the Hénon Map, $k = 6$, after convergence. The last Landau step used was with $\log_2 f_{min} = -14$ and $M = 256$ round-trips, from which these histograms were measured ($t_{min} = 5, t_{max} = 100$). Left panel: the histogram of proposals and total histogram on the initial conditions; compare with Fig. 1.7b. Right panel: the histogram of the escape time, showing flatness as required. Calculated escape time distribution on Fig. 3.2.

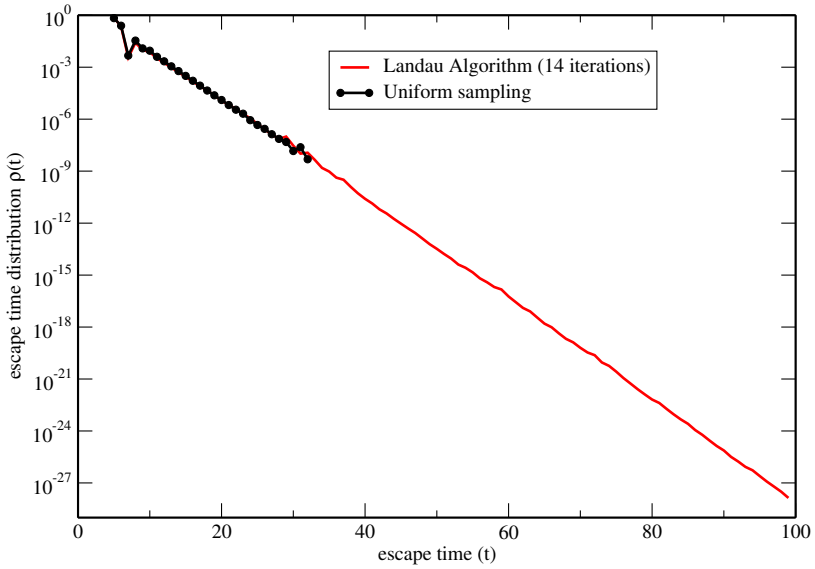

Figure 3.2: Escape time distribution of the hyperbolic Hénon map with $k = 6$ calculated using the two different methods. Black line with uniform sampling on the initial conditions, on red, using Landau algorithm with 14 steps. Both simulations used the same number of map iterations $\sim 10^8$. Histogram of the Landau algorithm are shown in Fig. 3.1.

higher escape times. From the $\rho(t)$ in Fig. 3.2, an uniform sampling would need in average $\sim 10^{27}$ samples to find one state with escape time 100; using the multicanonic algorithm, with $\sim 10^8$ samples we already have a very good estimation of $\rho(t = 100)$.

Given the successfull application of the method on these systems, and a clear improvement on the calculation of $\rho(t)$, we now focus on particular aspects of the method such as the understanding of the method in the context of dynamical systems, the relation of its free parameters (e.g. the proposal function) with the properties of the phase-space of a chaotic dynamical systems, and its limitations. So far, one question remains: why have we used an exponential decay on $\sigma(t)$, and why has that particular λ worked on that particular system? To answer this question, first we must understand a multicanonic simulation.

3.4 Mechanism of multicanonic simulation

For an efficient multicanonic simulation, the tunneling time must be as small as possible. For every $\boldsymbol{r}$, $t_e(\boldsymbol{r})$ is a function from the phase space to the escape time variable. This means that we can look at our Markov chain in the escape time variable, and consider it as a one-dimensional diffusion process in the escape time variable[51]. If the steps are local, $\Delta t \sim 1$, we expect that for a given sampling

interval $t_{max}-t_{min}$, the tunneling time to be of $O\left(\left(t_{max}-t_{min}\right)^2\right) \simeq O\left(t_{max}^2\right)$; a direct consequence of stochastic diffusion[50, 49]. This means that, ideally, this method would be of $O\left(t_{max}^2\right)$. However, the diffusivity is also dictated by the acceptance: proposed states that are rejected provide no diffusion in the random walk movement.

3.4.1 Acceptance of uniform proposal

To understand why the concept of locality is important in the random walk movement, and thus on the multicanonic simulation, we start considering an uniform proposal, $g\left(\boldsymbol{r} \to \boldsymbol{r}'\right) = 1/V$, which is clearly non-local. In this case we can analytically compute the acceptance. We start with Eq. 3.10,

$$A\left(\boldsymbol{r} \to \boldsymbol{r}'\right) = \min\left(1, \frac{p\left(\boldsymbol{r}'\right)}{p\left(\boldsymbol{r}\right)}\right) = \min\left(1, \frac{\rho\left(t_e\left(\boldsymbol{r}\right)\right)}{\rho\left(t_e\left(\boldsymbol{r}'\right)\right)}\right) \ .$$

To compute the acceptance on the escape time variable, we notice that the acceptance can be written as a conditional probability: $A\left(\boldsymbol{r} \to \boldsymbol{r}'\right) = P\left(\eta_A|\boldsymbol{r}', \boldsymbol{r}\right)$ where η_A is 1 if the accepted, and 0 if rejected. Bayes rule states that

$$P\left(\eta_A, \boldsymbol{r}'|\boldsymbol{r}\right) = P\left(\eta_A|\boldsymbol{r}', \boldsymbol{r}\right) P\left(\boldsymbol{r}'|\boldsymbol{r}\right) \ ,$$

and so we can write

$$A\left(\boldsymbol{r}\right) \equiv P\left(\eta_A|\boldsymbol{r}\right) = \int d\boldsymbol{r}' P\left(\eta_A|\boldsymbol{r}', \boldsymbol{r}\right) P\left(\boldsymbol{r}'|\boldsymbol{r}\right) \ .$$

Together with the fact that $P\left(\boldsymbol{r}'|\boldsymbol{r}\right) = g\left(\boldsymbol{r} \to \boldsymbol{r}'\right)$, we obtain

$$A\left(\boldsymbol{r}\right) = \int d\boldsymbol{r}' A\left(\boldsymbol{r} \to \boldsymbol{r}'\right) g\left(\boldsymbol{r} \to \boldsymbol{r}'\right) \ . \tag{3.12}$$

Averaging the acceptance over Ω, and using $g\left(\boldsymbol{r} \to \boldsymbol{r}'\right) = 1/V$, we obtain

$$\langle A \rangle\left(t\right) = \frac{1}{\rho\left(t\right)} \frac{1}{V} \int d\boldsymbol{r} A\left(\boldsymbol{r}\right) \delta_{t_e(\boldsymbol{r}),t} \ . \tag{3.13}$$

From Eq. 3.12 we have

$$A\left(\boldsymbol{r}\right) = \int d\boldsymbol{r}' \min\left(1, \frac{\rho\left(t_e\left(\boldsymbol{r}\right)\right)}{\rho\left(t_e\left(\boldsymbol{r}'\right)\right)}\right) \frac{1}{V} \ .$$

We can separate $A\left(\boldsymbol{r}\right)$ in two distinct cases to remove the min from the equation,

$$A\left(\boldsymbol{r}\right) = \frac{1}{V} \int d\boldsymbol{r}' \frac{\rho\left(t_e\left(\boldsymbol{r}\right)\right)}{\rho\left(t_e\left(\boldsymbol{r}'\right)\right)} H\left(t_e\left(\boldsymbol{r}'\right) < t_e\left(\boldsymbol{r}\right)\right) + \frac{1}{V} \int d\boldsymbol{r}' H\left(t_e\left(\boldsymbol{r}'\right) \geq t_e\left(\boldsymbol{r}\right)\right) \tag{3.14}$$

where $H(a)$ is 0 or 1 depending on a is false or true respectively. The second term is, from the definition of $\rho(t)$, given by

$$\frac{1}{V}\int d\boldsymbol{r}' H\left(t_e\left(\boldsymbol{r}'\right) \geq t_e\left(\boldsymbol{r}\right)\right) = \sum_{t'=t}^{\infty} \rho\left(t'\right) \ .$$

Inserting $A(\boldsymbol{r})$ of Eq. 3.14 on Eq. 3.13, we obtain

$$\langle A\rangle(t) = \frac{1}{\rho(t) V^2}\int d\boldsymbol{r}\int d\boldsymbol{r}' \frac{\rho(t)}{\rho\left(t_e\left(\boldsymbol{r}'\right)\right)} H\left(t_e\left(\boldsymbol{r}'\right) < t\right)\delta_{t_e(\boldsymbol{r}),t} + \sum_{t'=t}^{\infty}\rho\left(t'\right)$$

Integrating over $\boldsymbol{r}$, we have that

$$\langle A\rangle(t) = \frac{\rho(t)}{V}\int d\boldsymbol{r}' \frac{H\left(t_e\left(\boldsymbol{r}'\right) < t\right)}{\rho\left(t_e\left(\boldsymbol{r}'\right)\right)} + \sum_{t'=t}^{\infty}\rho\left(t'\right) \ .$$

Summing over t' restricted to $\delta_{t',t_e(\boldsymbol{r}')}$,

$$\frac{1}{V}\int d\boldsymbol{r}' \frac{H\left(t_e\left(\boldsymbol{r}'\right) < t\right)}{\rho\left(t_e\left(\boldsymbol{r}'\right)\right)} = \sum_{t'=1}^{\infty}\rho\left(t'\right)\frac{H\left(t' < t\right)}{\rho\left(t'\right)} \ ,$$

we obtain

$$\begin{aligned}\langle A\rangle(t) &= \rho(t)\sum_{t'=1}^{\infty}\rho\left(t'\right)\frac{H\left(t' < t\right)}{\rho\left(t'\right)} + \sum_{t'=t}^{\infty}\rho\left(t'\right) \\ &= \rho(t)(t-1) + \sum_{t'=t}^{\infty}\rho\left(t'\right) \ .\end{aligned}$$

For a hyperbolic open system, we have $\rho(t) = a\exp(-\gamma t)$ as mentioned in Sec. 1.3. In this case, we have

$$\begin{aligned}\langle A\rangle(t) &= a(t-1)e^{-\gamma t} - a\frac{e^{-\gamma t}}{e^{-\gamma}-1} \\ &= a(t-1)e^{-\gamma t} + a\frac{e^{-\gamma t}}{1-e^{-\gamma}} \\ &= ae^{-\gamma t}\left(t - 1 + \frac{1}{1-e^{-\gamma}}\right) \\ \langle A\rangle(t) &\sim e^{-\gamma t} \ .\end{aligned}$$

We see that if the proposal is non-local, the acceptance decays exponentially. This means that even if we can apply Landau algorithm to obtain $\rho(t)$, the number of proposals increases exponentially with the maximum time we want to sample which

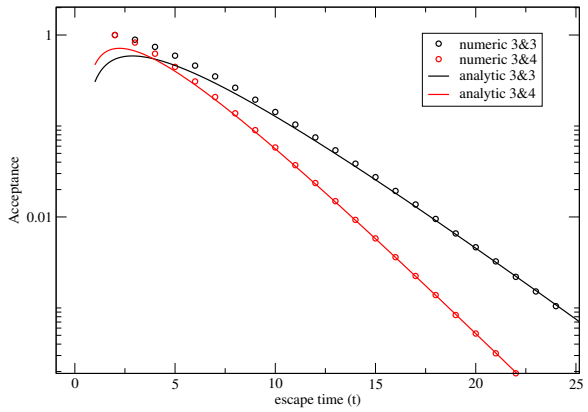

Figure 3.3: Exponential decay of the $A(t)$ for the open baker map with uniform proposals, for two different map parameters.

leads to an algorithm that increases exponentially with the maximum escape time, t_{max}, i.e. even if we can apply the Landau algorithm, it does not give any advantage over uniform sampling.

We confirm this behaviour in open baker map. In figure 3.3 we show the numerical and analytical comparison of the acceptance for the open baker map, showing the expected exponential decay.

3.4.2 Acceptance of local proposal

We now focus on a non-uniform proposal. Our objective is to connect the acceptance of the multicanonic simulation with the properties of the phase-space discussed in Chapter 1. We start with Eq. 3.12,

$$A(\boldsymbol{r}) \;=\; \frac{1}{V}\int d\boldsymbol{r}' \min\left(1, \frac{\rho(t)}{\rho(t')}\frac{g(\boldsymbol{r}'\to\boldsymbol{r})}{g(\boldsymbol{r}\to\boldsymbol{r}')}\right) g(\boldsymbol{r}\to\boldsymbol{r}') \;\;.$$

Now we can no longer apply a direct transformation to the time variable as we did in the uniform proposal, as now g depends explicitly in both $\boldsymbol{r}, \boldsymbol{r}'$. So, we assume that $g(\boldsymbol{r}\to\boldsymbol{r}')$ is a function only of $t_e(\boldsymbol{r})$ and $\varepsilon = |\boldsymbol{r}-\boldsymbol{r}'|$,

$$g(\boldsymbol{r}\to\boldsymbol{r}') = g(|\boldsymbol{r}-\boldsymbol{r}'|, t_e(\boldsymbol{r})) \;\;,$$

which is to say that we assume that we would like to use the concept of locality discussed before in the proposal function. With this assumption, we use Eq. 3.13 and multiply by $\delta(\varepsilon - |\boldsymbol{r}-\boldsymbol{r}'|)$, integrating over ε:

$$\langle A\rangle(t) = \frac{1}{\rho(t)V}\int d\varepsilon \int d\boldsymbol{r}\int d\boldsymbol{r}' \min\left(1, \frac{\rho(t)}{\rho(t'_e)}\frac{g(\varepsilon,t'_e)}{g(\varepsilon,t)}\right) g(\varepsilon,t)\,\delta(\varepsilon-|\boldsymbol{r}-\boldsymbol{r}'|)\,\delta_{t_e,t} \;\;.$$

We also sum on t'_e,

$$\langle A\rangle(t) = \frac{1}{\rho(t)\,V}\sum_{t'=0}^{\infty}\int d\varepsilon\int d\boldsymbol{r}\int d\boldsymbol{r}'\min\left(1,\frac{\rho(t)}{\rho(t')}\frac{g(\varepsilon,t')}{g(\varepsilon,t)}\right)g(\varepsilon,t)\,\delta\left(\varepsilon-|\boldsymbol{r}-\boldsymbol{r}'|\right)\delta_{t_e,t}\delta_{t'_e,t'}\ .$$

and we rearrange the terms:

$$\langle A\rangle(t) = \frac{1}{\rho(t)\,V}\sum_{t'=0}^{\infty}\int d\varepsilon\min\left(1,\frac{\rho(t)}{\rho(t')}\frac{g(\varepsilon,t')}{g(\varepsilon,t)}\right)g(\varepsilon,t)\int d\boldsymbol{r}\int d\boldsymbol{r}'\delta\left(\varepsilon-|\boldsymbol{r}-\boldsymbol{r}'|\right)\delta_{t_e,t}\delta_{t'_e,t'}\ .$$

We now define the quantity required in this calculation,

$$P_1(\varepsilon,t,t') = \frac{1}{V^2}\int d\boldsymbol{r}\int d\boldsymbol{r}'\delta\left(\varepsilon-|\boldsymbol{r}-\boldsymbol{r}'|\right)\delta_{t_e,t}\delta_{t'_e,t'}\ .$$

as the probability of picking two states, separated by ε, with escape times t and t'. We notice that this quantity is independent of the method; it only depends on the phase-space of the dynamical system. Assuming the approximation that if the proposed escape time is smaller than the present time, the steps will have an acceptance smaller than 1,

$$\frac{\rho(t)}{\rho(t')}\frac{g(\varepsilon,t')}{g(\varepsilon,t)} < 1\ \forall\varepsilon,\ t'<t$$

we can separate the two cases in the min() function and obtain

$$\langle A\rangle(t) \;=\; \frac{V}{\rho(t)}\left[\sum_{t'=0}^{t-1}\int d\varepsilon\frac{\rho(t)}{\rho(t')}g(\varepsilon,t')\,P_1(\varepsilon,t,t') + \sum_{t'=t}^{\infty}\int d\varepsilon g(\varepsilon,t)\,P_1(\varepsilon,t,t')\right]\ .$$

We notice that the first term is approximately zero as $\rho(t)/\rho(t')$ decays very fast with increasing $|t'-t|$. Hence, we are interested in the second term. If we imagine that g is very localized, we can approximate it by 1 within a distance ε from 0 and zero elsewhere. In that case, we would like to understand the cumulative version of P_1, $P(t'>t|t,\varepsilon)$, which has the same definition of P_1 but with the condition $|\boldsymbol{r}'-\boldsymbol{r}|<\varepsilon$, i.e. the probability to have a state $\boldsymbol{r}'$ with escape time $t'>t$ given that $|\boldsymbol{r}'-\boldsymbol{r}|<\varepsilon$ and that $\boldsymbol{r}$ has escape time t. Given their simplicity, we start to focus on hyperbolic systems.

3.5 Hyperbolic systems

Given the importance of the open baker map, introduced in section 1.1.4.1, and the analytical results that can be derived from it, we start our analysis on it. Our idea is to see how we can relate $P(t'>t|t,\varepsilon)$, defined in the previous section, with the properties of the phase-space.

We have seen that the open baker map asymptotically constructs its chaotic saddle, which is a Cantor set in the y direction. So, we can focus in the y direction only. *The set of states that escape at time t,* E_t, is recursively given by

$$E_t = cE_{t-1} \cup (1 - d + dE_{t-1}) \tag{3.15}$$

with $E_1 = [c, 1-d]$. *The set of points that escape at time* $t' \geq t$ is given recursively by

$$C_t = cC_{t-1} \cup (1 - d + dC_{t-1}) \tag{3.16}$$

with $C_1 = [0, 1]$. Both these sets are Cantor sets in the limit $t \to \infty$. We define the Cantor Heaviside Theta and Escape Heaviside Theta as

$$H_C(t, y) = \begin{cases} 1 & if\ y \in C_t \\ 0 & else \end{cases}\ ,\ H_E(t, y) = \begin{cases} 1 & if\ y \in E_t \\ 0 & else \end{cases}\ .$$

In figure 3.4 we represent both the $tH_C(t, y)$ and $tH_E(t, y)$ for the map 3&3. In this picture, $P(t' > t|t, \varepsilon)$ is the probability of, being at a given state y, with time t in Fig. 3.4(a), picking a state y' with $|y' - y| < \varepsilon$, with time $t' > t$. This condition is equivalent to t' being on a "tower" at $t + 1$ of 3.4(b). For instance, in figure 3.4 the four arrows represent the several possibilities to jump from one of the locations of $t = 2$. The total length of the set $[0, 1]$ that has escape time t is

$$L(t) = \int_0^1 H_E(t, y)\, dy = (c + d)^t (1 - c - d)\ , \tag{3.17}$$

and the probability to escape at time $t' > t$ can be calculated as

$$P(t' > t|t, \varepsilon) = \frac{1}{L(t)\,\varepsilon} \int_0^1 dy H_E(t, y) \int_{x-\varepsilon/2}^{x+\varepsilon/2} dy' H_C(t + 1, y') \tag{3.18}$$

i.e., we sum over all states y with time t, times the probability of an adjacent state y' have escape time $t' > t$. This can be seen as a convolution: we integrate $y \in [0, 1]$, and then $y' \in [y - \varepsilon, y + \varepsilon]$. In fact, this integration can be analytically computed, however, the number of branches scales exponentially with t. This happens because the number of different branches of both H_C and H_E scale with 2^t. So, we start to simplify this apparent complex problem.

Our simplified approach consists in estimating to what extent we really need to use all the terms of the integral. By looking at fig. 3.4, at each time, we can divide the several branches of H_E into *blocks*. We say that a block consists of a tower of time

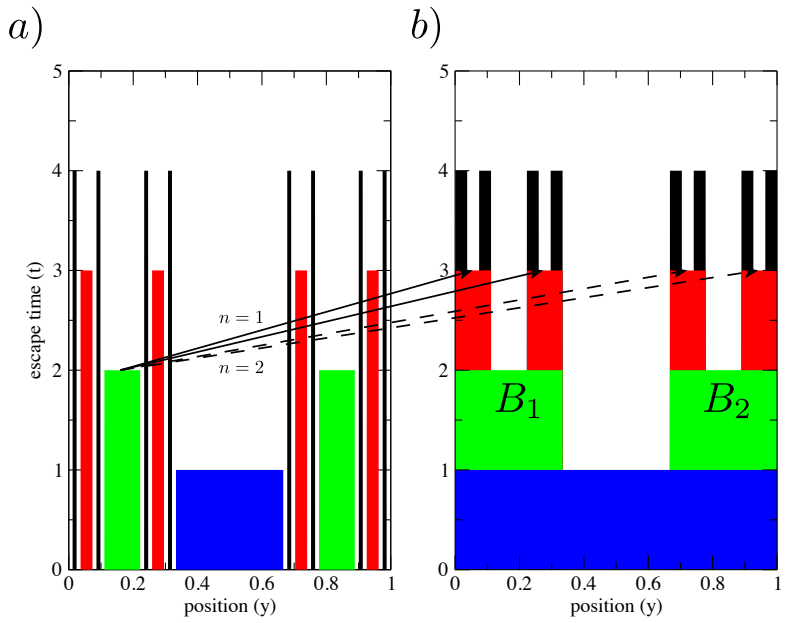

Figure 3.4: (Color) Construction of the Cantor set by the 3&3 open baker map; a) E_t, the set of points that escape at time t (set constructed in Fig. 1.6c); b) C_t, the set of points that escape at time $t' \geq t$. $t = 1, 2, 3, 4$ is represented by blue, green, red, black respectively. The arrows represent which jumps are allowed when taking the approximation $n = 1$ and $n = 2$ at time $t = 2$ (see text).

t in Fig 3.4(a), plus the two adjacent towers, with time $t+1$, at 3.4(b), as indicated by the filled arrows. For a fixed time t, each of the blocks has a characteristic length

$$l_k^t = c^k d^{t-k}$$

and our hypothesis is that, on a first approximation, the largest contribution to the integral comes from the immediate neighborhoods of the block. It is relevant to present a particular example of our reasoning: consider that we are at a state $\boldsymbol{r}$ with escape time $t = 2$. Looking at the figure 3.4(a), we are in one of the green towers. Lets assume, without loss of generality, that we are in the left one. Our hypothesis is that the integral 3.18 is dominated by the probability to jump to $\boldsymbol{r}'$ in one of the two left side red towers of figure 3.4(b), as indicated by the filled arrows. On this simplification we are neglecting the possible jumps indicated by the dashed arrows.

To study our hypothesis, we start by simplifying Eq. 3.18, substituting $H_C\left(t+1, y'\right)$ by

$$f\left(y', l\right) = \begin{cases} 1 & y' \geq 0 \wedge y' \leq lc \\ 1 & y' > l\left(1-d\right) \wedge y' \leq l \\ 0 & else \end{cases}$$

which is to say that we are only interested on the closest towers with $t' = t+1$. We catalog each of the blocks by B_i^t, where $i \in [1, N] = [1, 2^t]$. We can calculate

$$\tilde{P}\left(t' > t | B_i^t, t, \varepsilon\right) \equiv \frac{1}{l_i^t\left(1-c-d\right)\varepsilon} \int_{a \cdot l_i^t}^{l_i^t(1-d)} dy \int_{y-\varepsilon/2}^{y+\varepsilon/2} f\left(y', l_i^t\right) dy' \ ,$$

which we call the $n = 1$ *order approximation of the probability to jump to* $t' > t$*, given that we are at escape time* t*, at block* B_i^t *and with a fix* ε*.* We can use this quantity and Bayes' rule,

$$\tilde{P}\left(t' > t, B_i | t, \varepsilon\right) = \tilde{P}\left(t' > t | B_i, t, \varepsilon\right) \tilde{P}\left(B_i | t, \varepsilon\right)$$

to compute

$$\tilde{P}\left(t' > t | t, \varepsilon\right) \ = \ \sum_{i=1}^{2^t} \tilde{P}\left(t' > t, B_i | t, \varepsilon\right) \tilde{P}\left(B_i | t, \varepsilon\right) \ .$$

The probability$\tilde{P}\left(B_i | t, \varepsilon\right) = \tilde{P}\left(B_i | t\right)$ is just the probability to be in the block B_i with escape time t, which is proportional to the length of that block times the fraction that is at time t:

$$\begin{aligned} \tilde{P}\left(B_i | t, \varepsilon\right) &= \frac{l_i^t\left(1-c-d\right)}{\sum_{k=0}^{N} l_k^t\left(1-c-d\right)} \\ &= \frac{l_i^t}{\sum_{k=1}^{N} l_k^t} \ . \end{aligned}$$

On the other hand, the number of blocks with length $l_k^t = c^k d^{t-k}$ is given by the binomial distribution. Because $P\left(t' > t, l_k^t | t, \varepsilon\right) = P\left(t' > t, B_k^t | t, \varepsilon\right)$ and

$$\frac{L\left(t\right)}{\left(1-c-d\right)} = \left(c+d\right)^t = \sum_{i=1}^{2^t} l_i^t = \sum_{k=0}^{t} \left(\begin{array}{c} t \\ k \end{array} \right) c^k d^{t-k}$$

we obtain

$$\tilde{P}\left(t' > t | t, \varepsilon\right) = \frac{\left(1-c-d\right)}{L\left(t^*\right)} \sum_{k=0}^{t^*} \left(\begin{array}{c} t^* \\ k \end{array} \right) c^k d^{t^*-k} \tilde{P}\left(t' > t^*, l_k^{t^*} | t^*, \varepsilon\right) \tag{3.19}$$

where $t^* = t - 1$ comes from the fact that for $t = 1$ there is only one term on the sum, the one with length $l_0^0 = 1$.

In figure 3.5 we plot both $P\left(t' > t | t, \varepsilon\right)$ numerically calculated and the analytic $\tilde{P}\left(t' > t | t, \varepsilon\right)$, using Eq. 3.18 and 3.19 respectively, as a function of ε and for different t's for the symmetric 3&3 open baker map. For $\varepsilon \to 0$, $P\left(t' > t | t, \varepsilon\right) \to 0$ and the scaling is ε (in figure, it is a straight line with slope $m = 1$). This result is explained by the fact that for small ε, the region of interest is the border between the zone of escape time t (for $t = 2$, the red zone of fig. 3.4(a) and the zone $t' > t$ (green zone of fig. 3.4(b)). The scaling is due to the overlap of a window of size ε centered inside points of the zone of escape time t, which is ε. For $\varepsilon \to \infty$, $P\left(t' > t | t, \varepsilon\right) \to 0$, and the scaling is ε^{-1} (in figure, it is a straight line with slope $m = -1$). This result is explained by the fact that once ε is big enough, the integral is constant, but the normalization constant is proportional to ε.

The interesting result is that there exists an ε_{max} which maximizes $P\left(t' > t | t, \varepsilon\right)$. Moreover, an agreement of $\tilde{P}\left(t' > t | t, \varepsilon\right)$ with $P\left(t' > t | t, \varepsilon\right)$ is clear, showing that the dominant region for the integral is indeed the region within the block: the two lobes that appear in $t = 2$ are just the other two blue towers of figure 3.4, neglected in our simplification.

Another interesting discussion is that because the cantor set is self similar, the simplification taken is in fact a first order of a general method to compute $P\left(t' > t | t, \varepsilon\right)$; one can use a n'th order by considering 2^n towers. Because of self similarity, one concludes that the numerically calculated $P\left(t' > t | t, \varepsilon\right)$ for $t = 2$ is in fact the second order approximation for the $t = 2$: we took into account not only the two left most towers, but also the right ones (we counted both filled and dashed arrows in Fig. 3.4. This motivates the general formula to approximate $P\left(t' > t | t, \varepsilon\right)$:

$$P_n\left(t' > t | t, \varepsilon\right) = \frac{\left(1-c-d\right)}{L\left(t^*\right)} \sum_{k=0}^{t^*} \left(\begin{array}{c} t^* \\ k \end{array} \right) l_k^{t^*} P\left(t' > t^* | t^*, \varepsilon^*\right) \tag{3.20}$$

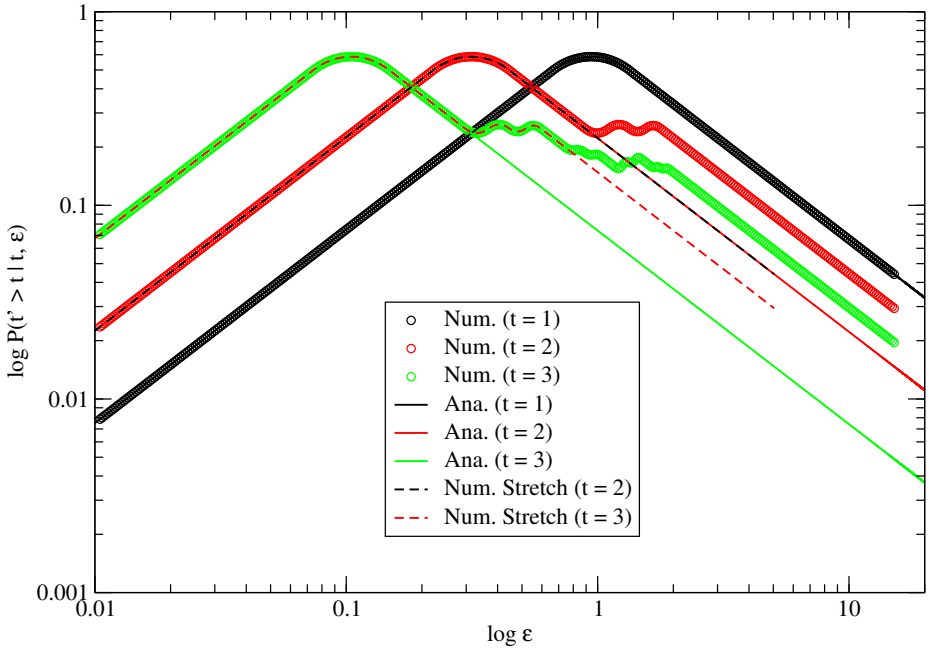

Figure 3.5: (Color) Probability distribution $P\left(t' > t|t, \varepsilon\right)$ and $\tilde{P}\left(t' > t|t, \varepsilon\right)$ as a function of ε, and for different escape times for the 3&3 open baker map. Thick lines showing the numerical result, obtained using Eq. 3.18, thin lines the analytical result using Eq. 3.19, and dashed lines the numericaly obtained result for t stretched by $1/3$, fitting parts of the $t-1$ curve.

with $t^* = t - n$ and $\varepsilon^* = \varepsilon / l_k^{t^*}$. For $t = n$, the result is exact. For $t > n$, the result is an approximation, which does not take into account all the terms of the integral Eq. 3.18. Because the evaluation of $P\left(t' > n | n, \varepsilon^*\right)$ is $O\left(2^n\right)$, the "heaviness" of the integral is constant for a fixed n, and the number of evaluations scales linearly with time because the number of terms of the sum scales with t. In figure 3.5 $P_n\left(t' > t | t, \varepsilon\right)$ is shown for $n = 1, t = 2$ in black dashed and $n = 2, t = 3$ in red dashed, confirming that the two lateral peaks on $t = 3$ are now covered by the $n = 2$ approximation.

3.5.1 The variation of $\varepsilon_{max}\left(t\right)$

One pertinent point at this stage is how the peak changes with the parameters. More importantly, it is relevant to understand how the peak calculated by the approximation $P_n\left(t' > t | t, \varepsilon\right)$ varies. The fact is that we cannot obtain $P\left(t' > t | t, \varepsilon\right)$ for $t \gg 1$ because the integration on Eq. 3.18 is numerically difficult. However, we can use the approximation $P_n\left(t' > t | t, \varepsilon\right)$, and estimate $\varepsilon_{max,n}\left(t\right)$. Our hypothesis is that $\varepsilon_{max,n}\left(t\right)$ is not very different from $\varepsilon_{max}\left(t\right)$. To verify this, we have calculated $\varepsilon_{max,n}\left(t\right)$ and $\varepsilon_{max}\left(t\right)$ for different n, t. Because we do not have access to $\varepsilon_{max}\left(t\right)$, the best we can do is to compare different n's.

We have performed the numerical integration of these quantities, using Mathematica® running on parallel, for three different orders, and we have found that the $\varepsilon_{max,n}\left(t\right)$ is the same (10^{-18} uncertainty), for both symmetric and non-symmetric maps, for $n = 1, 2, 3$, for t until 10 (which can be shown on the figure 3.8, as the numerically stretch line as the same maximum as the big lines. This result suggests that in fact the first order approximation is the one that dominates the variation of ε_{max}. A consequence of this result is that, for high enough t, the most probable towers of the phase-space with that escape time should dominate ε_{max}. This is because all the others become irrelevant in number and the fact that different sizes do not significantly contribute to the integral. Thus, the ε_{max} can be estimated as the length that maximizes the typical length at escape time t:

$$\hat{l}\left(t, k\right) = \frac{1}{\left(c + d\right)^t} \left(\begin{array}{c} t \\ k \end{array} \right) c^k d^{t-k} \ .$$

Maximizing $\hat{l}$ is the same as maximizing $\log \hat{l}$,

$$\begin{aligned} \log \hat{l}\left(t, k\right) &= \log\left(t!\right) - \log\left(k!\right) - \log\left(\left(t - k\right)!\right) \\ &+ k \log c + \left(t - k\right) \log d - t \log\left(c + d\right) \end{aligned}$$

which can be approximated, by Stirling's formula (which is valid for high t, exactly the limit we want to study), by

$$\begin{aligned}\log \hat{l}\,(t,k) &\simeq t\log(t) - k\log(k) - (t-k)\log(t-k) \\ &+ k\log c + (t-k)\log d - t\log(c+d)\ .\end{aligned}$$

Equating its derivative with respect to k to zero we obtain

$$\log\frac{t-k^*}{k^*} = \log\frac{d}{c}$$

or

$$k^* = \frac{t}{\frac{d}{c}+1}\ . \tag{3.21}$$

We can obtain ε_{max} by

$$\varepsilon_{max}(t) = c^{k^*} d^{t-k^*}$$

which, using Eq. 3.21, gives

$$\log\varepsilon_{max}(t) = -t\frac{c^{-1}\log d^{-1} + d^{-1}\log c^{-1}}{c^{-1}+d^{-1}}$$

Surprisingly,

$$\frac{c^{-1}\log d^{-1} + d^{-1}\log c^{-1}}{c^{-1}+d^{-1}} \equiv \lambda_L = \lambda_1$$

is the positive Lyapunov exponent of the open baker map (see Eq. 1.14). After the hard work, the result seems rather trivial: looking at two points in the phase-space separated by a distance ε, if one of the points has escape time t_1, for the second point to be in the same region (say of the order of the leak I) on time $t_2 \sim t_1$, then we must ensure that the divergence of their initial conditions after one more iteration must be compensated by a respective change on initial ε at $t = 0$. This divergence is given by the Lyapunov exponent (Sec. 1.1.4.1), and so the expected scaling of $\varepsilon_{max}(t)$ should be according to $\exp(-\lambda_L t)$.

Given the objective of achieving locality, we expect that $\sigma(t)$ should scale with $\varepsilon_{max}(t)$: if the proposal width is too big in a given time,

$$\sigma(t) \gg \varepsilon_{max}(t) \tag{3.22}$$

then, it approaches the limit $\sigma(t) \to \infty$ which is the uniform proposal treated in Sec. 3.4.1. The consequence is an acceptance going to zero. On the other hand, if

$$\sigma(t) \ll \varepsilon_{max}(t) \tag{3.23}$$

it is approaching the limit $\sigma(t) \to 0$ and the same escape time, $t' = t$, is always being proposed. The consequence is the acceptance going to one, but the simulation is stuck in a very specific region of the phase-space.

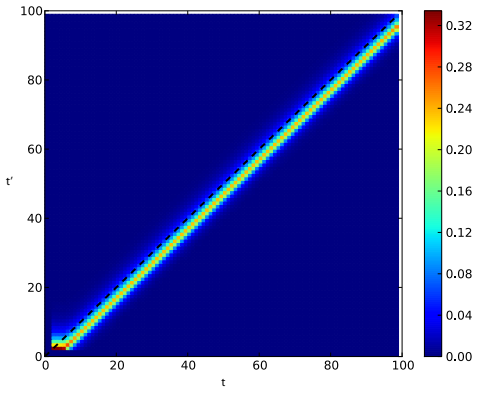

Figure 3.6: (Color) Probability of proposing t' given t for the 3&3 open baker map, calculated using exact density of states and $\lambda = \lambda_L$. Black dashed line represents the diagonal.

3.5.2 Computational verification

To confirm the scaling of $\sigma(t)$, we numerically apply the algorithm to the open baker map. All the simulations were made with the precision necessary so that $\sigma(t)$ is greater than the machine precision. Since a typical 64bits machine has only 19 decimal places when using long double, the GMP Multiple Precision Arithmetic Library[58] was used.

In figure 3.6 is shown the conditional probability of proposing a state with escape time t' given that the system is on a state with escape time t,

$$P(t'|t) \equiv M_{exc}(t, t')$$

also called the excitation matrix. This matrix was calculated using a "perfect" multicanonic simulation, i.e. using the exact density of states, $\rho(t) = \exp(-\gamma t)$, and the "exact" $\sigma(t) = a\exp(-\lambda_L t)$ in the 3&3 open baker map. The matrix is diagonal, meaning that we are effectively proposing states with high locality: we were able to find which $\varepsilon(t)$ leads to proposals with $\Delta t \sim 1$.

To further emphasize our result, in figure 3.7 we show the acceptance of a multicanonic simulation in the 3&3 and 3&9 open baker maps, for slightly different scalings of $\sigma(t)$. For a smaller exponent, $\lambda = 0.9\lambda_L$, the scaling of the typical ε_{max} is faster than the scaling of σ, causing a proposal of several states with time $t' < t$, as the situation of Eq. 3.23 is being more and more verified as $t \to \infty$. For higher exponent values, $\lambda = 1.1\lambda_L$, the scaling of ε_{max} is slower than that of σ, as we are approaching the situation of Eq.3.23 as $t \to \infty$. Finally, for adequate $\lambda = \lambda_L$, the acceptance is a constant quantity throughout the spectra.

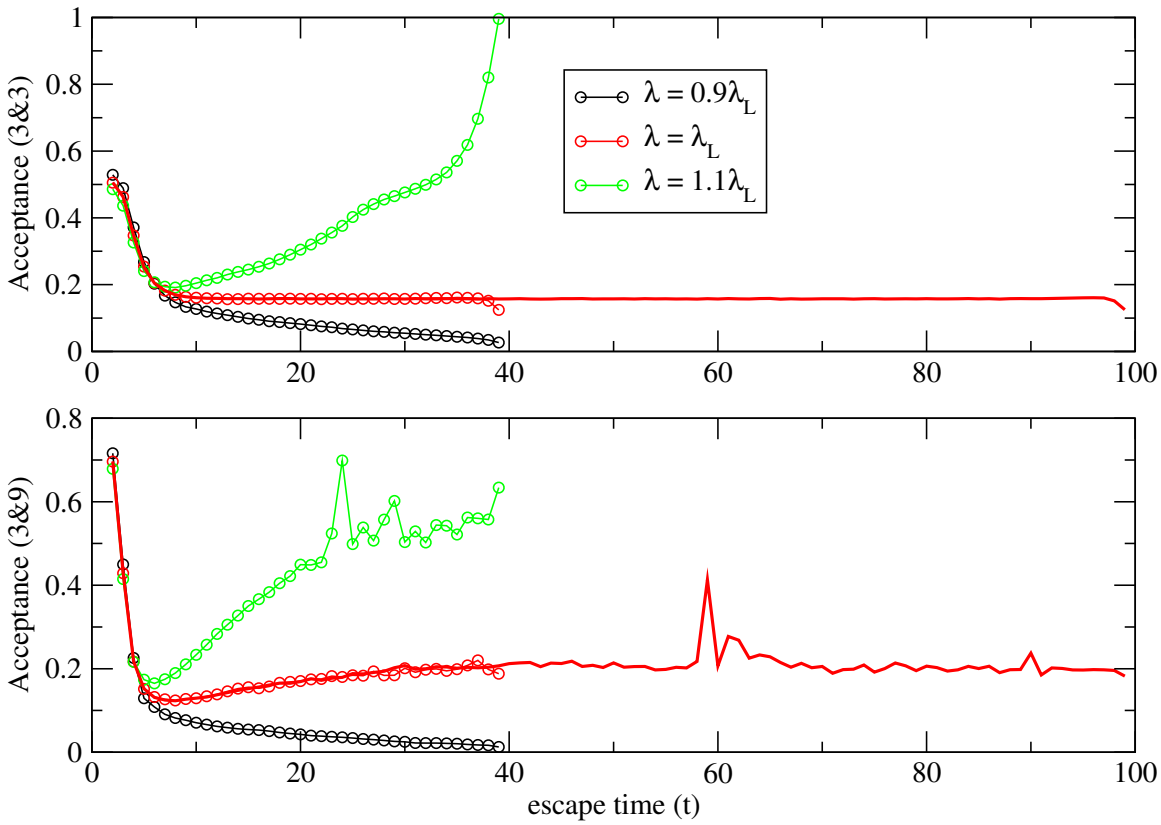

Figure 3.7: (Color online) Acceptance ratio vs escape time for the 3&3 and 3&9 open baker map, for a multicanonic simulation with proposal given by Eq. 3.10 with 3 different exponents. Thick line was calculated to $t_{max} = 100$.

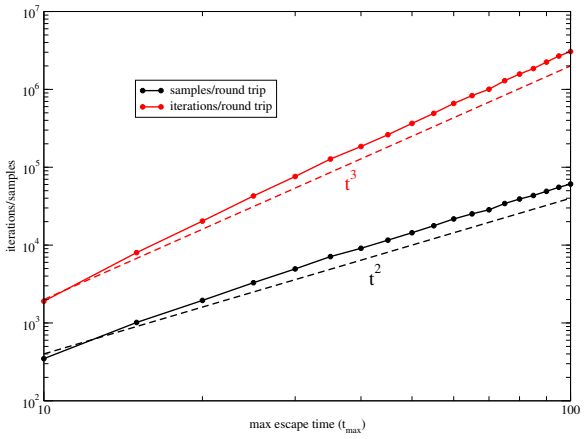

Figure 3.8: (Color Online) scaling of the tunneling time with maximum escape time t_{max} used. On both cases the scaling seems polimonial, and the coefficient in aparent agreement with predictions.

3.5.3 Efficiency of the algorithm

In Fig. 3.2, because the exponent of σ was adjusted to be close to the Lyapunov exponent, the acceptance is approximately constant. This leads to an algorithm that performs a random walk in the escape time variable with a constant diffusivity. The consequence is that the number of samples to estimate a given maximum escape time is of $O\left(t_{max}^2\right) \ll O\left(e^{\gamma t_{max}}\right)$, when compared to the uniform sampling. In figure 3.2 we showed $\rho\left(t\right)$ of the hyperbolic Hénon map, calculated using Landau's algorithm, with 10^8 samples. Notice that at $t_{max} = 100$, $\rho\left(t_{max}\right) \simeq 10^{-27}$, which would mean that, using an uniform sampling, 10^{27} samples would be needed to sample one point on which our algorithm is already giving a very good estimation.

To confirm the scaling of the algorithm, in figure 3.8 we present the number of samples and map iterations per round-trip as a function of the cutoff time t_{max}. The latter can be obtained by $tH\left(t\right)/N_{tt}$, where $H\left(t\right)$ is the measured histogram, and N_{tt} the number of round-trips used. As explained before, the number of samples should scale with t_{max}^2, and thus the map iterations should scale with t_{max}^3. Since the lack of decades makes difficult to tell if that it is in fact a power-law behavior, we restrict ourselves to mention that it seems a power law with exponent 2 for samples and 3 for iterations, in accordance with the theoretical predictions.

3.6 Adaptive method for computing the Lyapunov exponent

The previous discussion shows that the *a priori* knowledge of λ_L is a requirement for an efficient Monte Carlo simulation. This is a clear limitation of the Landau algorithm we have used. However, the previous discussion also showed that on an hyperbolic system, for each fixed t, if $\sigma(t) \gg \varepsilon_{max}(t)$, the proposals are mostly with $t' < t$ and that if $\sigma(t) \ll \varepsilon_{max}(t)$, most of the proposals are with $t' = t$. Motivated by this, we propose a generalization of the Landau algorithm.

Suppose we have no knowledge about the phase-space's structure of the hyperbolic system. In that case, our best guess would be to propose a state according to an uniform distribution, i.e. with a $\sigma(t)$ of the size of the phase-space maximum distances. After we proposed a state with that sigma, we gained the knowledge of which t' that particular $\sigma(t)$ gave. The results obtained in Sec. 3.5.1 suggest that, on average, if $t' < t$, we should decrease the $\sigma(t)$ the next time we are at that particular t. Likewise, if $t' \geq t$, we should increase $\sigma(t)$. So, we could adjust $\sigma(t)$ on the run, as it does not break the detailed balance of the Markov matrix.

Motivated by these ideas, we propose the following generalization of the Landau algorithm: consider a Landau scheme, where we also initialize $\sigma(t) = 1$ for $t \in [t_{min}, t_{max}]$. Every time we are in the state $\boldsymbol{r}$ with time t and we propose a state $\boldsymbol{r}'$ with time t', we do the following update:

$$\begin{cases} \sigma(t) \leftarrow \frac{\sigma(t)}{1+f} & \text{if } t' < t \\ \sigma(t) \leftarrow \sigma(t)(1+f) & \text{if } t' \geq t \\ S(t) \leftarrow S(t) + f\ . & \end{cases} \tag{3.24}$$

where f is the Landau's one and we use the same update of f, $f \leftarrow f/2$. Like in Landau algorithm, in the limit of $f \to 0$, we obtain a markovian process and thus we expect that $\sigma(t)$ converges to a quantity that is controlling the locality on each t.

In figure 3.9 we show $\sigma(t)$, $S(t) = \log \rho(t)$ and the histogram $H(t)$ of the last step of our method, for the open baker map for the 3&9, for 12 f-updates, with 128 round-trips each update of f. We find that the simple update scheme on Eq. 3.24 leads to a $\log \sigma(t) = -\lambda_{exp} t$. Notice that Eq. 3.24 does not imply any *a priori* exponential decay of the escape time. Also, the expected behavior of $S(t) \propto -\gamma_{sim} t$ is obtained. Using the analytical results from chapter 1, Eq. 1.14 and Eq. 1.12, a fit on both ρ and σ gives

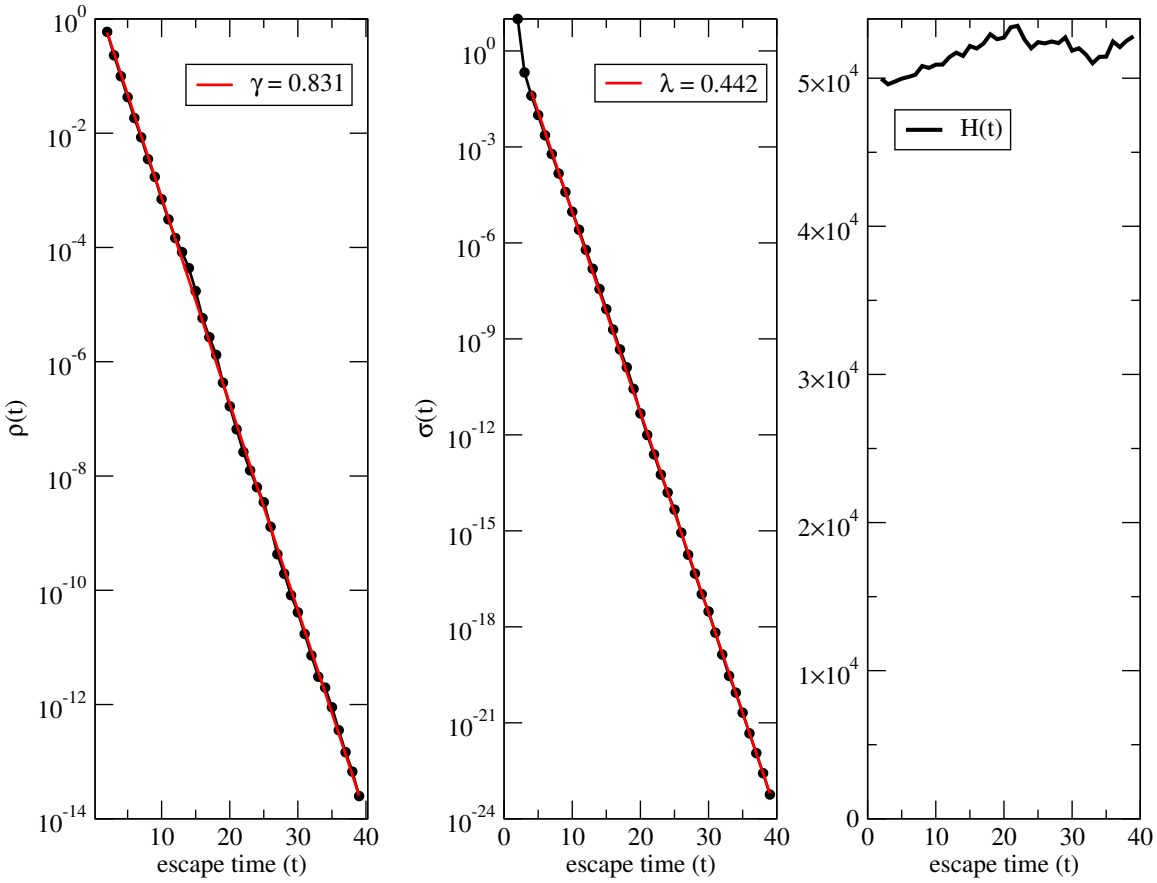

Figure 3.9: $\rho(t)$ and $\sigma(t)$ of the 3&9 Baker map calculated with our adaptive method. On the left, the escape time distribution, on the middle the $\sigma(t)$ built by our method. Also, on the right, the flat histogram of the last Landau step used. The reported values of the escape rate $\gamma = 0.831$ and the Lyapynov exponent $\lambda = 0.442$ were obtained by fitting the numerical results.

$$\frac{|\lambda_{exp} - \lambda_{exact}|}{\lambda_{exact}} = 0.001\%,\ 5.01\%$$

and

$$\frac{|\gamma_{exp} - \gamma_{exact}|}{\gamma_{exact}} = 0.164\%,\ 2.47\%$$

for the open 3&3 and 3&9 Baker map respectively. In the Hénon map with $k = 6$ (Eq. 1.16) there is no theoretical value for both γ and λ_L, but because for the Hénon map the metric entropy is $K_1 = \log 2$[17], from relation Eq. 1.15, we obtain

$$\lambda_L - \gamma = \log 2$$

A fit to both $\sigma(t)$ and $\rho(t)$ on the Hénon map gives

$$\frac{\lambda_{exp} - \gamma_{exp} - \log 2}{\log 2} = 3.00\% \ .$$

We confirm that both the acceptance and the conditional probability $P(t'|t)$ are constant and diagonal respectively, as expected. While a formal demonstration is not trivial for this non-markovian process, these results give important indications that the method is converging to $\sigma(t) \propto \exp(-\lambda_L t)$.

3.7 Higher dimensional systems

One important question left in the previous section is whether the methods that we are using are valid for higher dimensional hyperbolic systems. Probably the most important reason to ask this is because Monte Carlo integration is well known to be efficient in high dimensional systems[49, 50]. To test our method, we consider the 4-dimensional coupled Hénon Map[30, 17] defined by

$$T: \begin{cases} x_{n+1} &= A - x_n^2 + By_n + k(x_n - u_n) \\ y_{n+1} &= x_n \\ u_{n+1} &= C - u_n^2 + Dv_n + k(x_n - u_n) \\ v_{n+1} &= u_n \end{cases}$$

where A, B, C, D and k are parameters. For $A = 3$, $B = 0.3$, $C = 5$, $D = 0.3$, and $k = 0.4$ the map exhibits hyperbolic transient chaos, as studied in Ref. [30]. Taking the transient region to be bounded by $\overline{I} = [-4, 4] \times [-4, 4] \times [-4, 4] \times [-4, 4]$ (i.e. the initial conditions are inside $\overline{I}$, and the leak is defined if the particle leaves the region $\overline{I}$ [30]), we consider a straightforward generalization of the proposal of Eq. 3.10:

$$g(\boldsymbol{r} \to \boldsymbol{r}') = \prod_{i=1}^{4} g_i(\boldsymbol{r} \to \boldsymbol{r}')$$

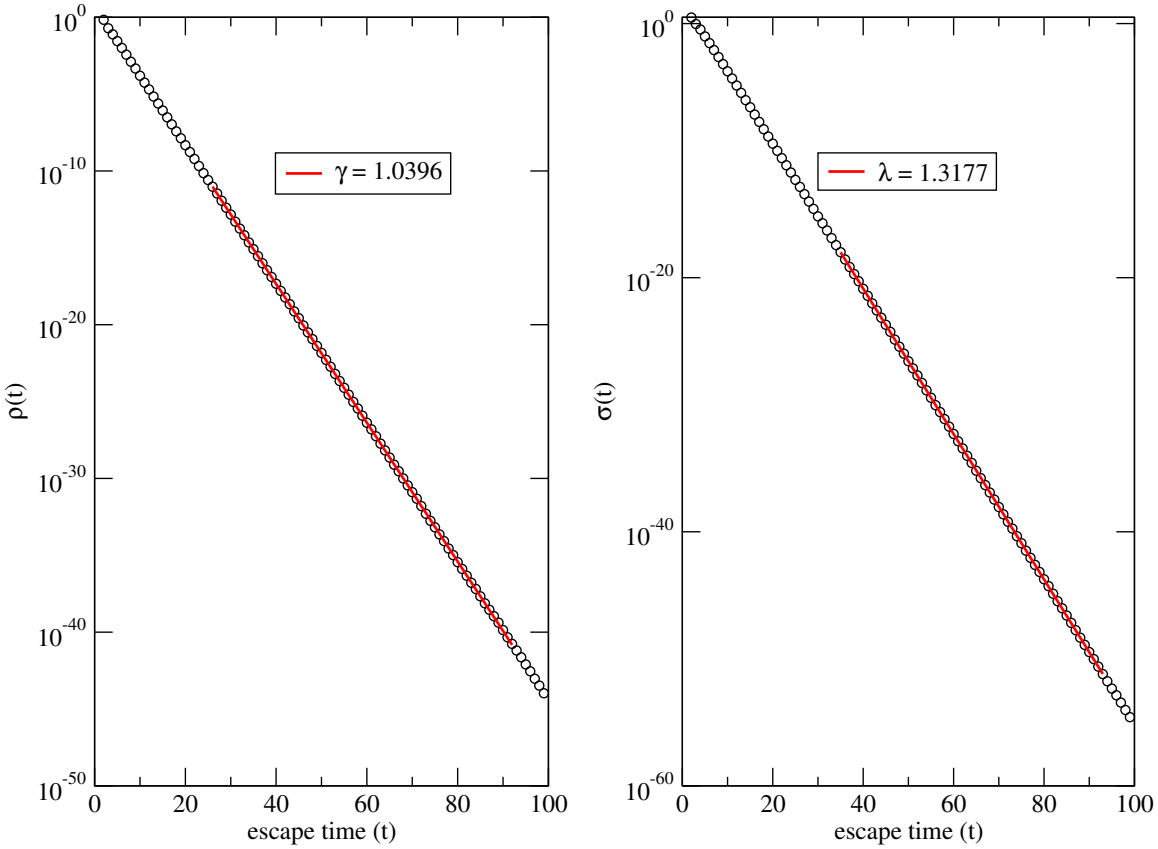

Figure 3.10: $\rho(t)$ and $\sigma(t)$ of the Coupled Hénon map, presented on text. On the left, the escape time distribution, on the right $\sigma(t)$ built by our method. Notice that the sampling is with probabilities as low as $\sim 10^{-45}$.

where

$$g_i(\boldsymbol{r} \to \boldsymbol{r}') = \mathcal{N}(|x_i - x_i'|, \sigma(t_e(\boldsymbol{r})))$$

i.e. a generalized Gaussian distribution, all with the same $\sigma(t)$. This is the only modification needed, which, in some sense, generalizes the proposal to a d dimensional space. In Fig. 3.10 $\rho(t)$ and $\sigma(t)$ obtained with our method are shown. The acceptance is again constant and the excitation matrix diagonal (Fig. 3.11) confirming the achieved locality. We have obtained

$$\lambda_{exp} = 1.318$$

well close to the maximum Lyapunov exponent obtained in Ref. [30], $\lambda_{ref} \approx 1.33$, suggesting that in higher dimensional systems, the quantity of interest for a constant acceptance is maximum Lyapunov exponent, closely approximated by our method.

We would like to emphatize that there is room for improvement in this generalization: a direction dependent proposal, $\boldsymbol{\sigma}(t) = (\sigma_x(t), \sigma_u(t))$ could be used. We

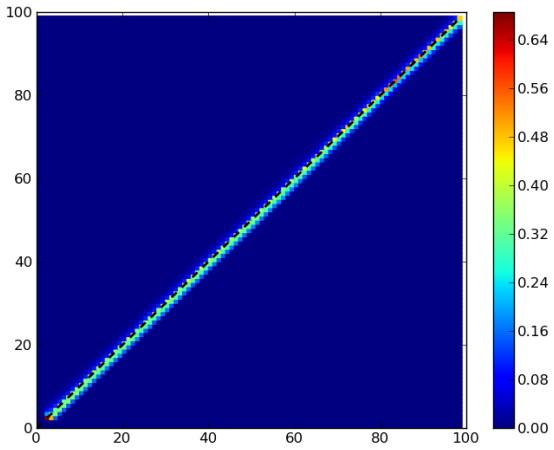

Figure 3.11: (Color) $P(t'|t)$ of the higher-dimensional Coupled Hénon map (see text for parameters) after our adaptive Landau algorithm converged. Diagonal ploted in black dashed. The matrix is clearly diagonal, showing the required locality.

believe that this choice, with a proper generalization of our adaptive method for more dimensions, could allow the calculation of the Lyapunov exponent's spectra. Nevertheless, as pointed out by Tamás Tél [59], this method allows the calculation of a very large set of points as close as one wishes from the chaotic saddle, as was done in Ref. [30]. Thus, important quantities of the saddle like the dimension spectra can be computed from them as well.

3.8 Non-hyperbolic systems

The most common Hamiltonian systems in physics are non-hyperbolic, as we discussed in chapter 1. We now focus in studying the possibilities of applying our method in non-hyperbolic open systems. We focus on one type of non-hyperbolic components, the KAM islands. We start by noticing that the assymptotic Lyapunov exponent of an non-hyperbolic Hamiltonian system tends to zero due to the stickiness around KAM islands. This means that the results in the previous section can not be applied to these systems. As we have discussed in Sec. 2.2.2, like the surviving probability, the escape time distribution has now three regimes related to the different components of the saddle.

By the same arguments used in Sec. 2.2.2, we would expect that the typical scales

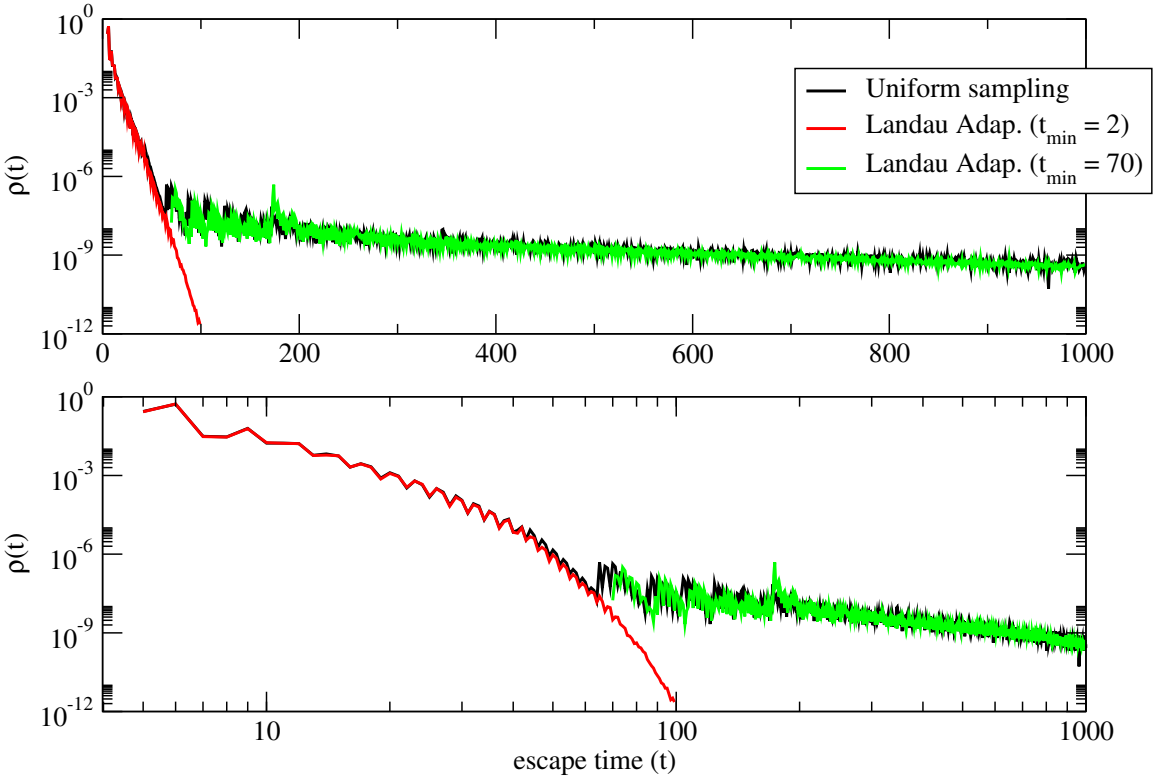

Figure 3.12: (Color) Escape time distribution for the non-hyperbolic Hénon map $k = 2$, for 2 different methods and different parameter, the minima of the spectra t_{min}. On top a log-linear scale, on botton a log-log scale. The transient time was estimated as $t_{II} \simeq 60$.

of the system, $\overline{\varepsilon}(t)$, be dominated by three regimes,

$$\overline{\varepsilon}(t) \approx \begin{cases} irregular & \text{for } t < t_I \\ Ae^{-\lambda_{eff}t} & \text{for } t_I < t < t_{II} \\ Bt^{-\alpha} & \text{for } t > t_{II}. \end{cases}$$

where λ_{eff} is an effective Lyapunov exponent and α a constant. One interesting point is whether our method converges when we apply it to a non-hyperbolic system. We apply the adaptive method to the non-hyperbolic Hénon map, Eq. 1.16 with $k = 2$. To compare the results regarding $\rho(t)$, we also compute $\rho(t)$ using an uniform sampling.

In figure 3.12 we show the escape time distribution of the studied map. In agreement with the discussion of Chapter 2, there is the expected transition time t_{II} from which $\rho(t)$ goes from exponential to power law behavior, shown in the uniform sampling (black line). However, the adaptive algorithm gives an unexpected result: if all the spectrum is considered (red line), the simulation converges to an exponential

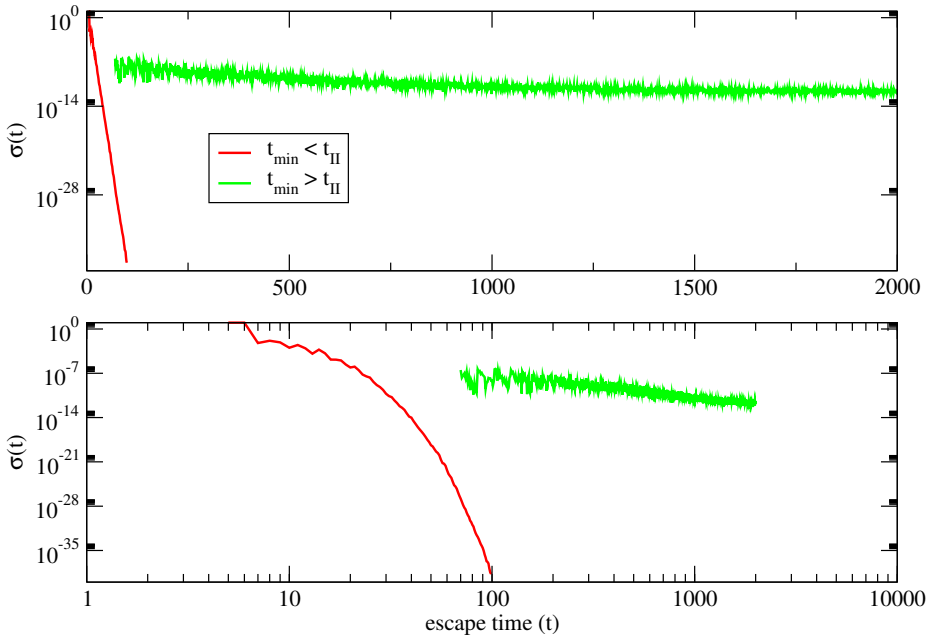

Figure 3.13: (Color) $\sigma(t)$ adaptively built by our method for the non-hyperbolic Hénon map $k = 2$, for two different simulations at different t_{min} (same simulations as on Fig. 3.12). On top a log-linear scale, on botton a log-log scale. A fit to the red curve gives $\lambda_{eff} = 0.957$.

decay of $\rho(t)$ for asymptotic time, which only fits the $\rho(t)$ obtained for uniform sampling for $t < t_{II}$. On the other hand, if the initial exponential decay is disregarded (i.e. $t_{min} = 70 > t_{II}$), the power-law behavior of $\rho(t)$ is obtained. This curve was multiplied by a constant to fit the uniform sampling: the fact that we are not considering $t < t_{min}$ leads to a different pre-factor on $\rho(t)$ because the sampling is on a smaller volume of the initial conditions; the original curve is shown in Fig. 3.14, black. The important point is that the scaling is consistent with the $\rho(t)$ obtained with uniform sampling.

In figure 3.13 we show $\sigma(t)$ after the convergence of the adaptive method for both situations: $t_{min} = 2 < t_{II}$ and $t_{min} = 70 > t_{II}$. As expected from the discussion of Chapter 2, when $t_{min} > t_{II}$ the scaling approaches a power-law. However, like in $\rho(t)$, the method with $t_{min} < t_{II}$ converges to an exponential decay of $\sigma(t)$. An important characteristic of the method with $t_{min} > t_{II}$ is that it does not fulfill ergodicity of the Markov process: because the round-trip is between t_{min} and t_{max}, and $\sigma(t_{min}) \sim 10^{-8}$, it is not guaranted that the system visits all the accessible initial conditions, $I_{initial}$.

One possibility to explain these results is the non-convergence of the adaptive method. The fact that we are changing both the proposal and the asymptotic distribution can lead to a Landau process that, only for very small f, makes the histogram

constant. Nevertheless, the entropy calculated should be a good approximation: the measured histogram on the last Landau step is approximately flat for both simulations and thus we are close to a markovian multicanonic process. Another alternative is bolder, and considers the following conjecture:

> there are regions of the phase-space responsible for the exponential decay, regions responsible for the power-law behavior and *these regions are not necessarily spatially related.*

Our conjecture is that we can spatially distinguish two types of dynamics (which we call regions): an "hyperbolic region", I_{exp}, responsible for the exponential decay of both $\rho(t)$ and $\sigma(t)$, and a "non-hyperbolic region", I_{pow}, responsible for the power-law decay of both $\rho(t)$ and $\sigma(t)$. Notice that these regions are fundamentally different from the regions considered in Sec. 1.2.1: the initial conditions start outside the KAM island.

To test our conjecture, we focus on explaining what we believe is happening on the adaptive method with $t_{min} < t_{II}$. Initially, it starts to build $\rho(t)$ and $\sigma(t)$ according to I_{exp}: it is the most likely region for $t < t_{II}$. Accordingly, $\sigma(t)$ is built to an exponential decay. When the system is at $t \sim t_{II}$, it is already highly correlated by the path it took to reach t. In particular, it came from the region I_{exp}. Because the proposals are governed by $\sigma(t) \sim \exp(-\lambda_{eff} t)$, the algorithm will only move in space with distances of scale of

$$\varepsilon \sim \varepsilon_{II} \equiv \exp(-\lambda_{eff} t_{II}) \ . \tag{3.25}$$

If the minimum distance from I_{exp} to I_{pow} is higher than ε_{II},

$$d_{min}(I_{exp}, I_{pow}) > \varepsilon_{II} \tag{3.26}$$

then, it is unlikely that there are proposals inside I_{pow}. This way, the algorithm continues on I_{exp}, and continues to build the exponential decay of $\rho(t > t_{II})$. In this view, we think that it is intuitive to think that it is converging to a "local hyperbolic escape time distribution",

$$\rho_{local,\,exp}(t) \propto e^{-\gamma t}$$

and a "local hyperbolic typical scaling",

$$\sigma_{local,\,exp}(t) \propto e^{-\lambda_{eff} t} \ .$$

From Fig. 3.13, we estimate $\lambda_{eff} \simeq 0.957$ and $t_{II} \simeq 60$, which leads, from Eq. 3.25 to

$$\varepsilon_{II} \sim 10^{-27} \ . \tag{3.27}$$

On the other hand, considering the other simulation, with $t_{min} > t_{II}$, we already start choosing the region to be the power-law region (because it is most likely to be chosen by the $\rho(t)$ obtained uniformly). So, the method does not fulfill the ergodicity condition and thus can become trapped on particular regions with escape times $t > t_{min}$, regions inside I_{pow}. So, it should converge to a "local non-hyperbolic escape time distribution",

$$\rho_{local,\,pow}(t) \propto t^{-\beta}$$

and a "local non-hyperbolic typical scaling",

$$\sigma_{local,\,pow}(t) \propto e^{-\alpha t} \ .$$

An interesting result suggesting this behavior is the observation of a very specific region

$$I_{local,pow} = [-2.5886082, -2.5886070] \subset I_{initial}$$

on which the adaptive method gets stuck in when $t_{min} > t_{II}$. Focusing on that region, an uniform sampling on it can be considered to compare with the adaptive algorithm. In figure 3.14 the escape time distribution is shown for both methods: in black the adaptive method using initial conditions inside $I_{initial}$ and $t_{min} = 70$, and in red the uniform sampling with initial conditions in $I_{local,pow}$ (this region does not have escape times smaller than 53). Clearly, both distributions agree for the times considered, suggesting that the adaptive method is actually calculating $\rho_{local,pow}(t)$, a consequence of not fulfilling ergodicity and being stuck in a region $I_{local,pow} \subset I_{pow}$. Nevertheless, this result suggests that the first part of the conjecture considered is correct: there is a defined region I_{pow} responsible for the power-law decay.

Finally, we notice that if there is an exponential decay region close to $I_{local,pow}$ (where closeness is given by Eq. 3.26) to where the method $t_{min} < t_{II}$ could jump from, then it should have been sampled when we used it (distribution given by the red line on figure 3.12). Interestingly, when we look to all the proposed points of that method after convergence, figure 3.15, we clearly see that it is proposing states with escape times $t \sim 100$ throughout the $I_{initial}$, as it should, but it is not proposing states nearby the region $I_{local,pow}$. Moreover, ε_{II} is clearly much smaller than the the distance from $I_{local,pow}$ to any region with high escape time on Fig. 3.15. This suggests that, indeed, the region $I_{local,pow}$ does not contain any exponential decay. Altogether,

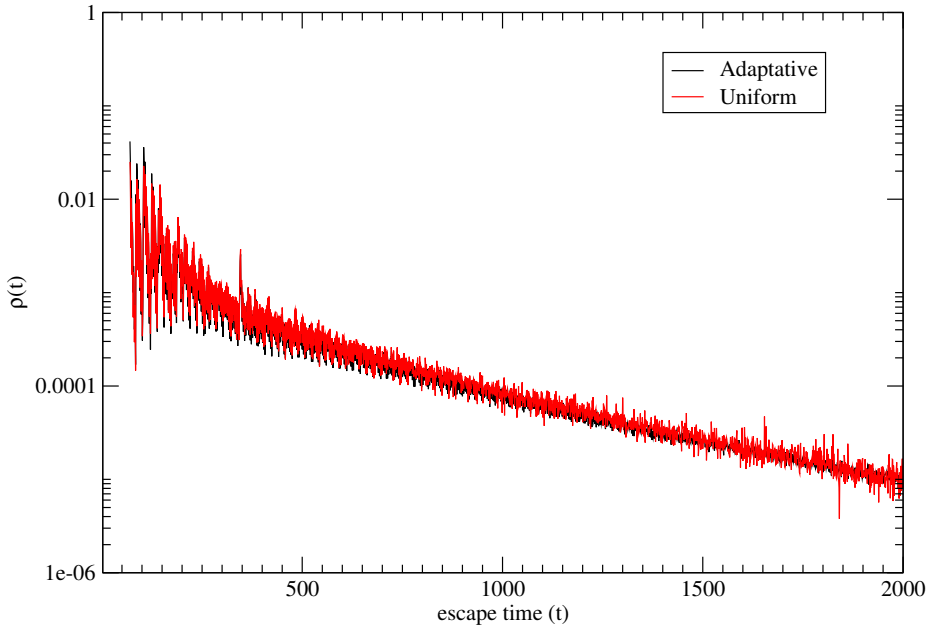

Figure 3.14: (Color Online) Escape time distribution for the non-hyperbolic Hénon map $k = 2$, for uniform sampling on $I_{local,pow}$ (red) and adaptive method on $I_{initial}$ with $t_{min} = 70$ (black), showing a clear agreement.

these results show that the application of our adaptive algorithm to non-hyperbolic systems is not straightforward. Our results suggest that important regions of the phase-space are being resolved. Future work is required to clarify how to extend our results of hyperbolic systems to mixed-phase-space systems.

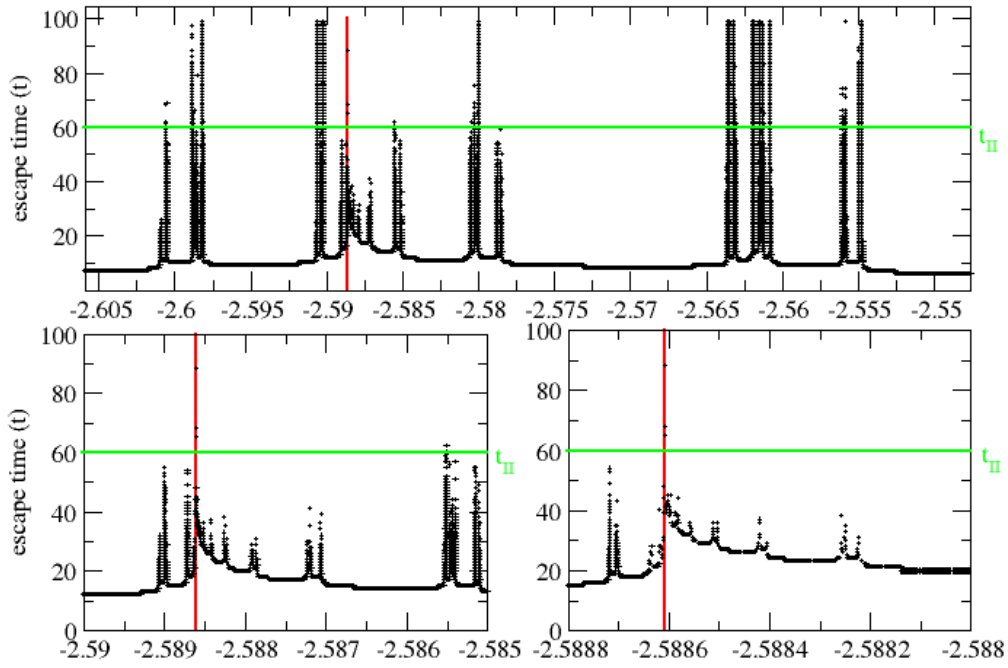

Figure 3.15: (Color Online) Escape time vs position $x \in I_{initial}$ proposed using the adaptive method after convergence, for $t_{min} < t_{II}$. Each point (out of 10^7 points) on the figure is a proposed state with the respective escape time and more than one round-trip was used to measure this figure. Red line is delimiting $I_{local,pow}$ (too small to distinguish the beginning and end of the region) and t_{II} in green line. Top image shows the relevant part of $I_{initial}$, bottom left a magnification of the top image and bottom right a magnification of the bottom left image. Looking at the region nearby $I_{local,pow}$, clearly almost no states were proposed on that region with escape time $t > t_{II}$. Notice that the distance from $I_{local,pow}$ to the biggest "tower" of the bottom right panel is $\sim 10^{-4} \gg \varepsilon_{II} = 10^{-27}$.

Chapter 4

Conclusions

In this thesis we studied transient chaos, which is mainly characterized by the properties of the chaotic saddle, such as the Lyapunov exponent, escape rate, fractal dimension, as introduced in chapter 1. We focused on the escape time distribution, both of hyperbolic and non-hyperbolic Hamiltonian systems. It is well known that the exponential decay of the escape time distribution is a signature of hyperbolic chaos. However, non-hyperbolic components lead to a power-law behaviour of the escape time distribution, which has important consequences on the long time behaviour of the trajectories. We introduced the complicated picture of KAM islands, and how they influence this power-law regime. In this thesis we have investigated the effect of noise on these systems and the question of an efficient procedure to sample initial conditions on then.

We have shown that noise-perturbed trajectories can lead to an even more intricate picture. While the survival probability turns exponential in all cases, as expected and previously noted, we characterized the existence of 5 intermediate regimes in non-hyperbolic systems. The parameters and the time-scale of these regimes were studied as a function of the leak size and noise intensity. We connected the phase-space components with those parameters and showed that the observed trapping of trajectories in Ref. [1] is also valid in mixed phase-space billiards. This result indicates that small perturbations in laser cavities may increase the transient regime. Finally, we have shown that the (intermediate-times) escape rate scales linearly with leak size and is extremely sensitive to the location of the leak, results previously known for fully chaotic systems[39, 40, 18]. Second, we have shown that the asymptotic exponential decay γ_ξ depends on the noise intensity, ξ, as $\gamma_\xi \sim \xi^2$ with a transition $\gamma_\xi = \gamma$ for large ξ, where γ is the escape rate of the non-perturbed system, Fig 2.5.

Even in simple systems like the ones we have considered, the computation effort to study transient chaos can be high. The exponential decay of the escape time distribu-

tion leads to a very difficult sampling of states with high escape times. In this thesis, we have used the analogy of the escape time distribution with the density of states used in statistical physics to introduce importance sampling techniques. With one of these techniques, the Landau algorithm[3], the escape time distribution is computed in polynomial time (Fig. 3.8), much faster than the exponential time generally verified for currently used methods (Fig. 3.2). By analytical calculations and numerical experiments, we have shown that the characteristic length of the proposal function of the sampling technique should scale exponentially in time, with exponent equal to the Lyapunov exponent. This allows us to achieve a polymonial computation time (Fig. 3.7). Motivated by this result, we introduced a generalization of the Landau algorithm to compute both the escape time distribution and the desired proposal function (Eq. 3.24). We have confirmed, by different numerical simulations, that our algorithm converges to a flat-histogram and flat-acceptance multicanonic simulation, both in lower and higher dimensional hyperbolic systems.

We would like to emphasize that a multicanonic simulation is extremely efficient and versatile, as it guarantees time-independent error bars of the measured quantities. Moreover, any quantity can be computed with it. One quantity usually referred in the literature is the visualization of the chaotic saddle[30, 60, 17]. Since our method already produces a large set of points with arbitrary high escape times, it can be used to compute the saddle directly[17, 59].

Finally, we apply our new techniques to non-hyperbolic systems. We have shown that the adaptive method we developed (and thus the Landau algorithm) converges either to the exponential decay or the power-law regime (Fig. 3.12). Using our algorithm, we reported that, for the paradigmatic system we have studied, there are specific regions of the phase-space, away from the non-hyperbolic components of the chaotic saddle, that only have the power-law regime (Fig. 3.15). This suggests that the hyperbolic and non-hyperbolic components of the chaotic saddle are not mixed in the phase-space. We numerically confirm that an uniform sampling on these power-law regions allows the calculation of, at least, four more decades of the power-law tail (Fig. 3.14 and Fig. 3.12). It is an open issue whether these regions are particular of the studied map or if this is a general property of non-hyperbolic systems.

To our knowledge, the use of Monte Carlo techniques to sample a phase space with fractal structure is new. This leads to several questions. Are there better distributions to use for the proposal function? This non-convergence of our algorithm suggests that the Landau algorithm also fails to converge. Is the non-convergence of

the Landau algorithm general in non-hyperbolic systems? We think this is the first time a non-convergence of the Landau algorithm is reported.

Finally, we would like to emphasize that the two apparently distinct topics studied in this thesis are in fact very close to each other: on one hand, random perturbations lead to a random walk in the phase space, which causes the trajectory to become trapped in non-hyperbolic components of the phase space. On the other hand, the Monte Carlo technique uses a random walk in the phase-space to better approach the chaotic saddle. In both cases, the key elements arise from the interplay between a complicated deterministic dynamics and a simple stochastic process. The results are simpler in hyperbolic systems and more difficult in non-hyperbolic cases. Altogether, the results of this thesis show that the combination of methods and algorithms of statistical physics can lead to more efficient numerical procedures and an improved understanding of transiently chaotic systems.

References

[1] E. G. Altmann and A. Endler. Noise-Enhanced Trapping in Chaotic Scattering. *Physical Review Letters*, 105(24):255102, 2010.

[2] E. G. Altmann, J. C. Leitão, and J. Viana Lopes. Effect of noise in open chaotic billiards. *Chaos*, 22(2):026114, June 2012.

[3] F. G. Wang and D. P. Landau. Determining the density of states for classical statistical models: A random walk algorithm to produce a flat histogram. *Physical Review E*, 64:056101, 2001.

[4] E. Ott. *Chaos in Dynamical Systems*. Cambridge University Press, Cambridge, 2nd edition, 1993.

[5] N. Chernov and R. Markarian. *Chaotic Billiards*. American Mathematical Society, 2006.

[6] J. D. Meiss. Symplectic maps, variational principles, and transport. *Reviews of Modern Physics*, 64(3):795–848, July 1992.

[7] J. C. Leitão. On the Search of Solitons of the Discrete Non-Linear Schrödinger Equation. Technical report, Departamento de Física da Faculdade de Ciências da Universidade do Porto, Porto, 2012.

[8] S. Smale. Differentiable dynamical systems,. *Bulletin American Mathematic Society*, 73, 1967.

[9] J. D. Meiss and E. Ott. Markov Tree Model of Transport in Area-Preserving Maps. *Physica D*, 20(2-3):387–402, 1986.

[10] J. D. Meiss. Average exit time for volume-preserving maps. *Chaos*, 7(1):139–147, 1997.

[11] G. Cristadoro and R. Ketzmerick. Universality of algebraic decays in Hamiltonian systems. *Physical Review Letters*, 100(18):184101, 2008.

[12] R. Venegeroles. Universality of Algebraic Laws in Hamiltonian Systems. *Physical Review Letters*, 102(6):64101, 2009.

[13] B. V. Chirikov and D. L. Shepelyansky. Correlation-Properties of Dynamical Chaos in Hamiltonian-Systems. *Physica D*, 13(3):395–400, 1984.

[14] G. M. Zaslavsky. Chaos, fractional kinetics, and anomalous transport. *Physics Reports-Review Section of Physics Letters*, 371(6):461–580, 2002.

[15] E. G. Altmann. *Intermittent Chaos in Hamiltonian Dynamical Systems*. PhD thesis, University of Wuppertal, 2007.

[16] E. G. Altmann, T. Friedrich, A. E. Motter, H. Kantz, and A. Richter. Prevalence of marginally unstable periodic orbits in chaotic billiards. *Physical Review E*, 77(1):16205, 2008.

[17] Y.-C. Lai and T. Tél. *Transient chaos: Complex dynamics in finite time scales*, volume 173. Springer, New York, 1st edition, 2010.

[18] E. G. Altmann and T. Tél. Poincaré recurrences and transient chaos in systems with leaks. *Physical Review E*, 79(1):16204, 2009.

[19] A. J. Fendrik, A. M. F. Rivas, and M. J. Sanchez. Decay of quasibounded classical Hamiltonian systems and their internal dynamics. *Physical Review E*, 50(3):1948–1958, 1994.

[20] C. P. Dettmann and O. Georgiou. Quantifying intermittency in the open Drive-belt billiard. *Chaos*, 22(2):026113, 2012.

[21] C. P. Dettmann and O. Georgiou. Survival probability for the stadium billiard. *Physica D-Nonlinear Phenomena*, 238(23-24):2395–2403, 2009.

[22] C. Jung, T. Tél, and E. Ziemniak. Application of scattering chaos to particle transport in a hydrodynamical flow. *Chaos*, 3(4):555–568, 1993.

[23] S. Shinohara, M. Hentschel, J. Wiersig, T. Sasaki, and T. Harayama. Ray-wave correspondence in limaçon-shaped semiconductor microcavities. *Physical Review A*, 80(3), September 2009.

[24] Q. Song, L. Ge, A. Stone, H. Cao, J. Wiersig, J.-B. Shim, J. Unterhinninghofen, W. Fang, and G. Solomon. Directional Laser Emission from a Wavelength-Scale Chaotic Microcavity. *Physical Review Letters*, 105(10), August 2010.

[25] T. Harayama and S. Shinohara. Two-dimensional microcavity lasers. *Laser and Photonics Reviews*, 5(2):247–271, 2011.

[26] E. G. Altmann. Emission from dielectric cavities in terms of invariant sets of the chaotic ray dynamics. *Physical Review A*, 79:013830, 2009.

[27] E. G. Altmann, A. E. Motter, and H. Kantz. Stickiness in mushroom billiards. *Chaos*, 15(3), 2005.

[28] M. S. Custódio and M. W. Beims. Intrinsic stickiness and chaos in open integrable billiards: Tiny border effects. *Physical Review E*, 83(5):056201, 2011.

[29] M. Hentschel and K. Richter. Quantum chaos in optical systems: The annular billiard. *Physical Review E*, 66(5):56207, 2002.

[30] D. Sweet, H. E. Nusse, and J. A. Yorke. Stagger-and-step method: detecting and computing chaotic saddles in higher dimensions. *Physical Review Letters*, 86(11):2261–2264, 2001.

[31] N. Saitô, H. Hirooka, J. Ford, F. Vivaldi, and G. H. Walker. Numerical Study of Billiard Motion in an Annulus bounded by Non-Concentric Circles. *Physica D*, 5(2-3):273–286, 1982.

[32] A. Akaishi and A. Shudo. Accumulation of unstable periodic orbits and the stickiness in the two-dimensional piecewise linear map. *Physical Review E*, 80(6):66211, 2009.

[33] C. P. Dettmann and O. Georgiou. Open mushrooms: stickiness revisited. *Journal of Physics A:Mathematical and Theoretical*, 44(19):195102, 2011.

[34] Y. C. Chen. On topological entropy of billiard tables with small inner scatterers. *Advances in Mathematics*, 224(2):432–460, 2010.

[35] C. Foltin. Billiards with positive topological entropy. *Nonlinearity*, 15:2053, 2002.

[36] O. Bohigas, D. Boose, R. E. de Carvalho, and V. Marvulle. Quantum Tunneling and Chaotic Dynamics. *Nuclear Physics A*, 560(1):197–210, 1993.

[37] R. E. de Carvalho, C. V. Abud, and F. C. Souza. Dissipation as a mechanism of energy gain. *Physical Review E*, 77(3):36204, 2008.

[38] G. Pianigiani and J. A. Yorke. Expanding Maps on Sets Which are Almost Invariant - Decay and Chaos. *Transactions of the American Mathematical Society*, 252(AUG):351–366, 1979.

[39] V. Paar and N. Pavin. Bursts in average lifetime of transients for chaotic logistic map with a hole. *Physical Review E*, 55(4):4112–4115, 1997.

[40] L. A. Bunimovich and C. P. Dettmann. Peeping at chaos: Nondestructive monitoring of chaotic systems by measuring long-time escape rates. *Epl*, 80:40001, 2007.

[41] E. G. Altmann, J. S. E. Portela, and T. Tél. Leaking Chaotic Systems. *(in preparation)*, 2011.

[42] E. G. Altmann and H. Kantz. Hypothesis of strong chaos and anomalous diffusion in coupled symplectic maps. *Epl*, 78(1), 2007.

[43] A. Kruscha. Destruction of Invariant Tori under Symplectic Random Perturbation. *Diplomarbeit, TU Dresden (Germany)*, 2011.

[44] C. S. Rodrigues, A. P. S. de Moura, and C. Grebogi. Random fluctuation leads to forbidden escape of particles. *Physical Review E*, 82(2):26211, 2010.

[45] I. V. Pogorelov and H. E. Kandrup. Noise-induced phase space transport in two-dimensional Hamiltonian systems. *Physical Review E*, 60(2):1567–1578, 1999.

[46] A. Kruscha, R. Ketzmerick, and H. Kantz. Biased diffusion inside regular islands under random symplectic perturbations. *Physical Review E*, 85(6), 2012.

[47] W. Feller. *An introduction to probability theory and its applications*. John Willey and Sons, New York, 1950.

[48] E. Floriani, R. Mannella, and P. Grigolini. Noise-induced transition from anomalous to ordinary diffusion: The crossover time as a function of noise intensity. *Physical Review E*, 52(6):5910–5917, 1995.

[49] M. E. J. Newman and G. T. Barkema. *Monte Carlo Methods in Statistical Physics*. Oxford University Press, USA, New York, April 2002.

[50] C. P. Robert and G. Casella. *Monte Carlo statistical methods*. Springer texts in statistics. Springer, Berlin, 2nd edition, 2005.

[51] J. Viana Lopes. *Métodos de Monte Carlo para sistemas com desordem e interacção de longo alcance*. PhD thesis, Universidade do Porto, 2006.

[52] N. Metropolis, A. W. Rosenbluth, M. N. Rosenbluth, A. H. Teller, and E. Teller. Equation of State Calculations by Fast Computing Machines. *The Journal of Chemical Physics*, 21(6):1087, June 1953.

[53] B. Berg and T. Neuhaus. Multicanonical ensemble: A new approach to simulate first-order phase transitions. *Physical Review Letters*, 68(1):9–12, January 1992.

[54] R. E. Belardinelli and V. D. Pereyra. Wang-Landau algorithm: a theoretical analysis of the saturation of the error. *The Journal of chemical physics*, 127(18):184105, November 2007.

[55] R. E. Belardinelli and V. D. Pereyra. Fast algorithm to calculate density of states. *Physical Review E*, 75:046701, 2007.

[56] S. Trebst, D. A. Huse, and M. Troyer. Optimizing the ensemble for equilibration in broad-histogram Monte Carlo simulations. *Physical Review E*, 70:046701, 2004.

[57] P. Dayal, S. Trebst, S. Wessel, D. Wurtz, M. Troyer, S. Sabhapandit, and S. N. Coppersmith. Performance limitations of flat-histogram methods. *Physical Review Letters*, 92(9):097201, 2004.

[58] T. Granlund and the GMP development Team. GNU MP: The GNU Multiple Precision Arithmetic Library, 2012.

[59] T. Tél. Private Talk, 2012.

[60] E. M. Bollt. The Path Towards a Longer Life: on Invariant Sets and the Escape Time Landascape. *International Journal of Bifurcation and Chaos*, 15(5):1615–1624, 2005.